



## OPEN Novel, soluble 3-heteroaryl-substituted tanshinone mimics attenuate the inflammatory response in murine macrophages

Elisa Facen<sup>1,8</sup>, Giulia Assoni<sup>1,2,7,8</sup>, Greta Donati<sup>3</sup>, Dalila Paladino<sup>1</sup>, Agata Carreira<sup>1</sup>, Isabelle Bonomo<sup>1</sup>, Valeria La Pietra<sup>3</sup>, Roberta Lotti<sup>4</sup>, Josef Houser<sup>5</sup>, Luca L. Fava<sup>1</sup>, Pierfausto Seneci<sup>2</sup>, Luciana Marinelli<sup>3</sup>✉, Daniela Arosio<sup>6</sup>✉ & Alessandro Provenzani<sup>1</sup>✉

The RNA binding protein Human Antigen R (HuR) has been identified as a main regulator of the innate immune response and its inhibition can lead to beneficial anti-inflammatory effects. To this aim, we previously synthesized a novel class of small molecules named Tanshinone Mimics (TMs) able to interfere with HuR-RNA binding, and that dampen the LPS-induced immune response. Herein, we present a novel series of TMs, encompassing thiophene 3/TM9 and 4/TM10, furan 5/TM11 and 6/TM12, pyrrole 7b/TM13, and pyrazole 8. The furan-containing 5(TM11) showed the greatest inhibitory effect of the series on HuR-RNA complex formation, as suggested by RNA Electromobility Shift Assay and Time-Resolved FRET. Molecular Dynamics Calculation of HuR – 5/TM11 interaction, quantum mechanics approaches and Surface Plasmon Resonance data, all indicates that, within the novel heteroaryl substituents, the furan ring better recapitulates the chemical features of the RNA bound to HuR. Compound 5/TM11 also showed improved aqueous solubility compared to previously reported TMs. Real-time monitoring of cell growth and flow cytometry analyses showed that 5/TM11 preferentially reduced cell proliferation rather than apoptosis in murine macrophages at immunomodulatory doses. We observed its effects on the innate immune response triggered by lipopolysaccharide (LPS) in macrophages, showing that 5/TM11 significantly reduced the expression of proinflammatory cytokines as *Cxcl10* and *Il1b*.

**Keywords** ELAVL1, HuR, LPS, HuR inhibitors, Anti-inflammatory agents, Tanshinone mimics

Inflammation is a pivotal part of the non-specific defence mechanisms orchestrated by the innate immune system and represents a fundamental response to counteract biological, physical, and chemical threats<sup>1</sup>. One of the most potent stimuli triggering an inflammatory response in macrophages is LipoPolySaccharide (LPS), a ubiquitous component of Gram-negative bacterial membranes. LPS has strong macrophage-activating properties<sup>2</sup> and is widely used in laboratory models to mimic inflammatory conditions. It induces the production of various inflammatory cytokines, including but not limited to IL-1 $\beta$ , IL6, and IL8<sup>3</sup>. Such cytokines are tightly regulated at the post-transcriptional level by RNA Binding Proteins (RBPs) such as TTP<sup>4</sup>, HuR<sup>5</sup> and TIAR<sup>6–8</sup>. The Human Antigen R (HuR or ELAVL1), a member of the ELAVL family, embodies the multifaceted role of RBPs, participating in diverse processes including organismal development<sup>9</sup>, cell growth<sup>10</sup>, inflammation<sup>11,12</sup>. HuR is ubiquitously expressed in human tissues and strongly conserved among mammals<sup>13</sup>. Structurally, HuR contains three RNA Recognition Motifs (RRMs), with RRM1 and RRM2 cooperatively responsible for RNA binding. Upon RNA interaction, RRM1 and RRM2 undergo a conformational change towards a closed,

<sup>1</sup>Department of Cellular, Computational and Integrative Biology (CIBIO), University of Trento, Via Sommarive 9, Trento 38123, Italy. <sup>2</sup>Department of Chemistry, University of Milan, Via Golgi 19, Milan 20133, Italy. <sup>3</sup>Department of Pharmacy, University of Napoli Federico II, Via D. Montesano 49, Napoli 80131, Italy. <sup>4</sup>DERMOLAB, University of Modena and Reggio Emilia, via del Pozzo, 71, Modena 41124, Italy. <sup>5</sup>Central European Institute of Technology, Masaryk University, Kamenice 753/5, Brno 625 00, Czech Republic. <sup>6</sup>Istituto di Scienze e Tecnologie Chimiche (SCITEC) 'Giulio Natta', Consiglio Nazionale delle Ricerche (CNR), Via C. Golgi 19, Milan 20133, Italy. <sup>7</sup>Present address: Department of Chemistry and Applied Biosciences, ETH Hoenggerberg, HCI H498, Zurich 8093, Switzerland. <sup>8</sup>These authors contributed equally: Elisa Facen and Giulia Assoni. ✉email: Imarinel@unina.it; daniela.arosio@scitec.cnr.it; alessandro.provenzani@unitn.it

positively charged conformation conducive to RNA binding<sup>14</sup>. HuR specifically binds to AU/U-rich elements, often located within the 3' UnTranslated Region (3' UTR) of its target RNAs<sup>15</sup>. Remarkably, these sequences are present in approximately 7% of the human transcriptome, underscoring the HuR's involvement in diverse cellular processes. Previous studies have demonstrated that HuR inhibitors can control inflammation and attenuate LPS-driven response in murine macrophages<sup>16</sup>, as well as to reduce nephritis<sup>17</sup>. Taken together, these studies suggest that targeting HuR is a valuable strategy to fine-tune the inflammatory response. Indeed, HuR represents an appealing and promising target for therapeutic strategies<sup>18</sup>. Reported approaches for targeting HuR include the use of small interfering RNAs (siRNAs) and small molecule inhibitors<sup>13,19</sup>. The landscape of the latter HuR inhibitors is diverse, including molecules such as naturally occurring naphthofuranone MS-444<sup>22</sup>, the naturally inspired, coumarin-like CMLD2<sup>23</sup>, and the synthetic, benzothiophene-centered KH-3<sup>24</sup>. Despite the profusion of strategies to find HuR inhibitors, they still face major issues, such as limited solubility and bioavailability, as well as off-target effects on other ELAVL proteins and RBPs<sup>25</sup>. Therefore, targeting this RBP remains a major challenge in biomedical research. Along the same line, we recently reported a series of Tanshinone Mimics (TMs) that interact with the RRM1 and RRM2 domains of HuR<sup>20</sup>, affecting its activity<sup>21</sup>. Although in our previous effort, we introduced ortho substituents on the 3-phenyl ring of the 3-aryl-1,3-TM system to disrupt the rings' planarity and improve aqueous solubility<sup>16</sup>, this approach still yielded unsatisfactory results.

Herein, we further enriched the family of TMs with new members by functionalizing position 3 with polar heterocycles. With this aim, we synthesized a small array of polar 3-heteroaryl substituted TMs. Among these, we selected and characterized 3-(2-furyl) 5 / TM11, showing an improved aqueous solubility compared to its analogs and previous leads 1 / TM6a and 2 / TM7n. We provide a comprehensive biochemical profile of 5 / TM11, complemented by investigations into its ability to counteract the LPS-induced inflammatory response in murine macrophages, and its impact on cell cycle progression. Computational techniques and quantum-mechanic approaches were employed to unravel the binding mode of 5 / TM11 within HuR and to understand the differences in binding potency among 5 / TM11 and its analogs.

## Results and discussion

### Synthesis of 3-heteroaryl substituted TMs

Naturally occurring Dihydro-tanshinone I (DHTS-I, Fig. 1), a HuR inhibitor able to prevent its stabilizing interaction with multiple mRNAs and endowed with cytotoxic cellular activity<sup>21</sup>, inspired our function-oriented synthesis of a small array of bicyclic indole-sulfonamide Tanshinone Mimics (TMs). Among these, 1 / TM6a (Fig. 1) showed a higher affinity for HuR in comparison to natural DHTS-I and was selected as an early lead<sup>20</sup>. Further expansion of the TM library led to 7-substituted 2 / TM7n (Fig. 1), obtained by introducing a 2,6'-dimethylphenyl substituent in position 3 through a Suzuki coupling and adding a 4-methoxyphenyl-thiol in position 7 by Michael addition. This new ligand was characterized by slightly improved solubility in in vivo-compatible media, allowing for its evaluation in an LPS-induced inflammation model<sup>16</sup>.

To further improve the drug-likeness of TM HuR inhibitors, we focused on replacing the 3-phenyl ring with 5-membered heterocycles (i.e., thiophene 3 / TM9 and 4 / TM10, furan 5 / TM11 and 6 / TM12, pyrrole 7a, 7b / TM13, and pyrazole 8, Fig. 2). These modifications aimed to enhance hydrophilicity, primarily due to the presence of heteroatoms<sup>26</sup>. Larger or bicyclic ring systems were not considered, as their bulkiness could impair HuR binding for the resulting ligands<sup>20</sup>.

Our synthesis of 3-heteroaryl-containing TMs followed the optimized synthetic strategy previously reported for TMs<sup>20</sup>, successfully leading to synthetic targets 3–6 and 7b / TM9–13 (Fig. 3). Namely, Suzuki coupling of bromophenol 9<sup>20</sup> with commercially available boronic acids or dioxaborolanes, catalyzed by palladium(0) tetrakis or 1,1'-bis(diphenylphosphino)ferrocene palladium(II)dichloride respectively, allowed the synthesis of intermediate ethers 10–15 in good yields (step a – 10–14, or b – 15, Scheme 1). For the pyrazole derivative 15, commercially available *N*-Boc-protected pyrrole 2-boronic acid was employed to avoid any interference due to the free NH group. Methoxyindoles 10–15 were then demethylated (step c) using 1 M BBr<sub>3</sub> in dry DCM, yielding free phenols 14–20a and 21. The low yield obtained for intermediate 18 was probably due to furan polymerization induced by the strong acidic conditions required for ether cleavage, which also led to Boc deprotection for pyrrole intermediate 20a. Lastly, oxidation of phenols 16–19 and 21 was performed under standard IBX oxidation conditions (step d, Scheme 1), yielding target heteroaryl-containing TMs 3–6 / TM9–12 in overall good yields. Unfortunately, when oxidation was attempted on intermediates 20a and 21, TLC monitoring and UPLC-MS analysis showed complex reaction mixtures and the absence of the desired

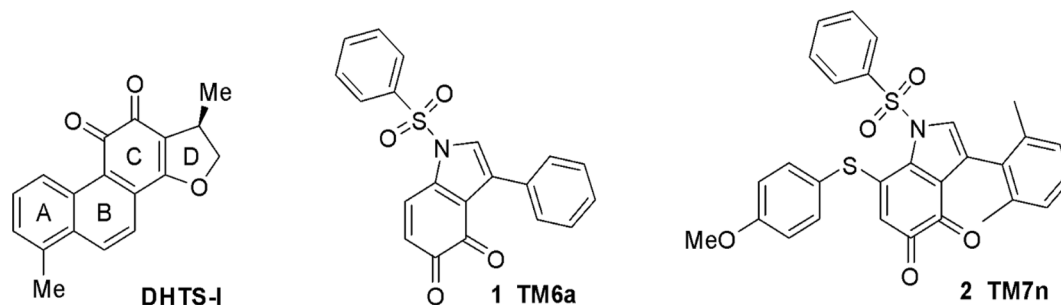


**Fig. 1.** Chemical structure of naturally occurring DHTS I, and early leads 1/TM6a and 2/TM7n.

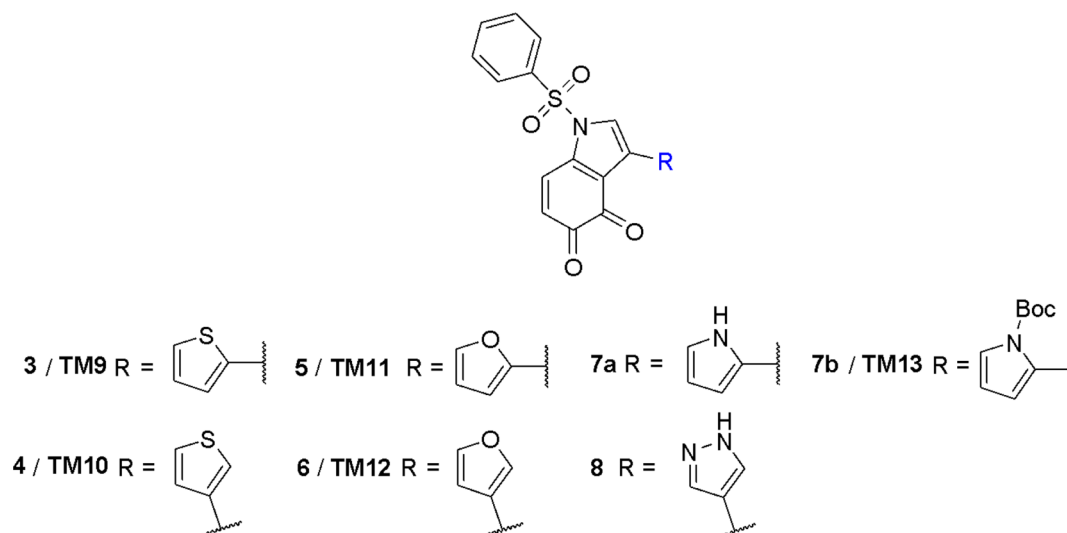


**Fig. 2.** Chemical structure of targeted 3-heteroaryl-containing tanshinone mimics 3–8(TM9–13).

product, probably due to oxidation-dependent side reactions of the free NH groups in pyrrole and pyrazole rings. Protection of the pyrrole **20a** with Boc enabled its oxidation and led to the formation of the Boc-protected pyrrole-derivative **7b** / **TM13**; unfortunately, removing the Boc protecting group was unsuccessful in multiple experimental protocols. Further efforts towards synthesizing pyrrole- and pyrazole-containing targets **7a** and **9** will be the subject of future communication. Target heteroaryl TMs **3–6** / **TM9–12**, together with the Boc-protected pyrrole derivative **7b** / **TM13** were then submitted to biological evaluation.

### Biochemical profiling

We initially challenged 3-heteroaryl substituted TMs for their ability to disrupt the HuR-RNA interaction *in vitro* by a RNA Electrophoretic Mobility Shift Assay (REMSA) screen. The first two RRM domains of human HuR, expressed in *Escherichia coli* BL21 as recombinant M1M2 (rM1M2), were incubated with an AU-rich 26-nucleotide RNA probe linked at 5' to the DY681 fluorophore for complex formation. Then TMs **3–6**, **7b** / **TM9–13** were added at 15  $\mu\text{M}$ , and the reaction mixture was run in a polyacrylamide gel. 3-(2-Furyl) **5** / **TM11** showed the greatest inhibitory effect on HuR-RNA complex formation (Fig. 3A). Subsequently, we confirmed its potency with a dose-response curve (Fig. 3B), determining its half-maximal inhibitory concentration ( $\text{IC}_{50}$ ) to be 0.77  $\mu\text{M}$  (Fig. 3C). TM congeners **3** / **TM9**, **4** / **TM10**, **6** / **TM12** and **7b** / **TM13** showed lower potencies, with  $\text{IC}_{50}$  values ranging from 1.8 to 13  $\mu\text{M}$  (Supplementary Fig. S1). To precisely quantify the  $\text{IC}_{50}$  of **5** / **TM11**, we employed a Homogeneous Time-Resolved Fluorescence (HTRF) assay<sup>27,28</sup>, utilizing a previously reported 26-nucleotide AU-rich biotinylated probe<sup>16</sup>. We determined an  $\text{IC}_{50}$  value of 0.68  $\mu\text{M}$  (Fig. 3D) for **5** / **TM11**, showing similar potency to **2** / **TM7n** (0.79  $\mu\text{M}$ )<sup>16</sup>. We then calculated the affinity interaction of **2** / **TM7n** and **5** / **TM11** by surface plasmon resonance (SPR), showing apparent  $K_D$ s in the low micromolar range for both TMs, with slightly better values for **5** / **TM11** (**2** / **TM7n**  $K_D = 8.59 \pm 1.70$   $\mu\text{M}$ , **5** / **TM11**  $K_D = 3.34 \pm 1.48$   $\mu\text{M}$ , Fig. 3E, Supplementary Fig. S2). Next, we evaluated the aqueous solubility of **5** / **TM11** using kinetic solubility measurements [liquid chromatography–mass spectrometry (LC-MS)] in PBS with increasing quantities of DMSO. **5** / **TM11** was solubilized at 21.25  $\mu\text{M}$  in PBS-5% DMSO and 31.25  $\mu\text{M}$  with 20% DMSO (Fig. 3F), resulting to be ten times more soluble than **2** / **TM7n** or **1** / **TM6a** (2.9  $\mu\text{M}$  or 4.2  $\mu\text{M}$  with 20% DMSO, respectively)<sup>16</sup>. Overall, heterocyclic **5** / **TM11** has shown a slightly better inhibitory activity in disrupting the binding of HuR with target mRNAs and improved solubility with respect to **2** / **TM7n**.

### 5/TM11-HuR binding mode investigation

#### Molecular docking and molecular dynamics simulations of 5/TM11-HuR binding mode

We performed molecular docking simulations to elucidate the binding mode of **5** / **TM11** with HuR. Given the intrinsic complexity of the HuR binding pocket, due to the highly flexible RRM1-RRM2 interdomain region, we employed two docking software, Glide and Autodock4.2 (see Computational Methods for further details). Simulations performed with Autodock basically converged on two poses (Lowest Energy and most populated one, Supplementary Fig. S3) which were well superimposable to the first and second lowest poses in energy predicted by Glide. A close inspection of both poses showed that **5** / **TM11** occupies the central RRM1-RRM2 interdomain region, although with a different spatial orientation (Supplementary Fig. S3). To probe the stability of these binding modes, we performed a 1.5  $\mu\text{s}$  long simulation run for each of the two binding modes. As a result, we found that one pose (Pose A, largest cluster of Autodock, and first in energy of Glide) remains tightly bound to the protein (see ligand RMSD in Fig. 4), stabilizing the HuR RRM domains in a closed conformation (see time-evolution of the RRM1-RRM2 center of mass (CoM) distance). The other conformation (Pose B), conversely, did not retain a stable binding and turned out in the opening of the RRM1-RRM2 domain (Supplementary Fig. S4), thus it was not considered further.

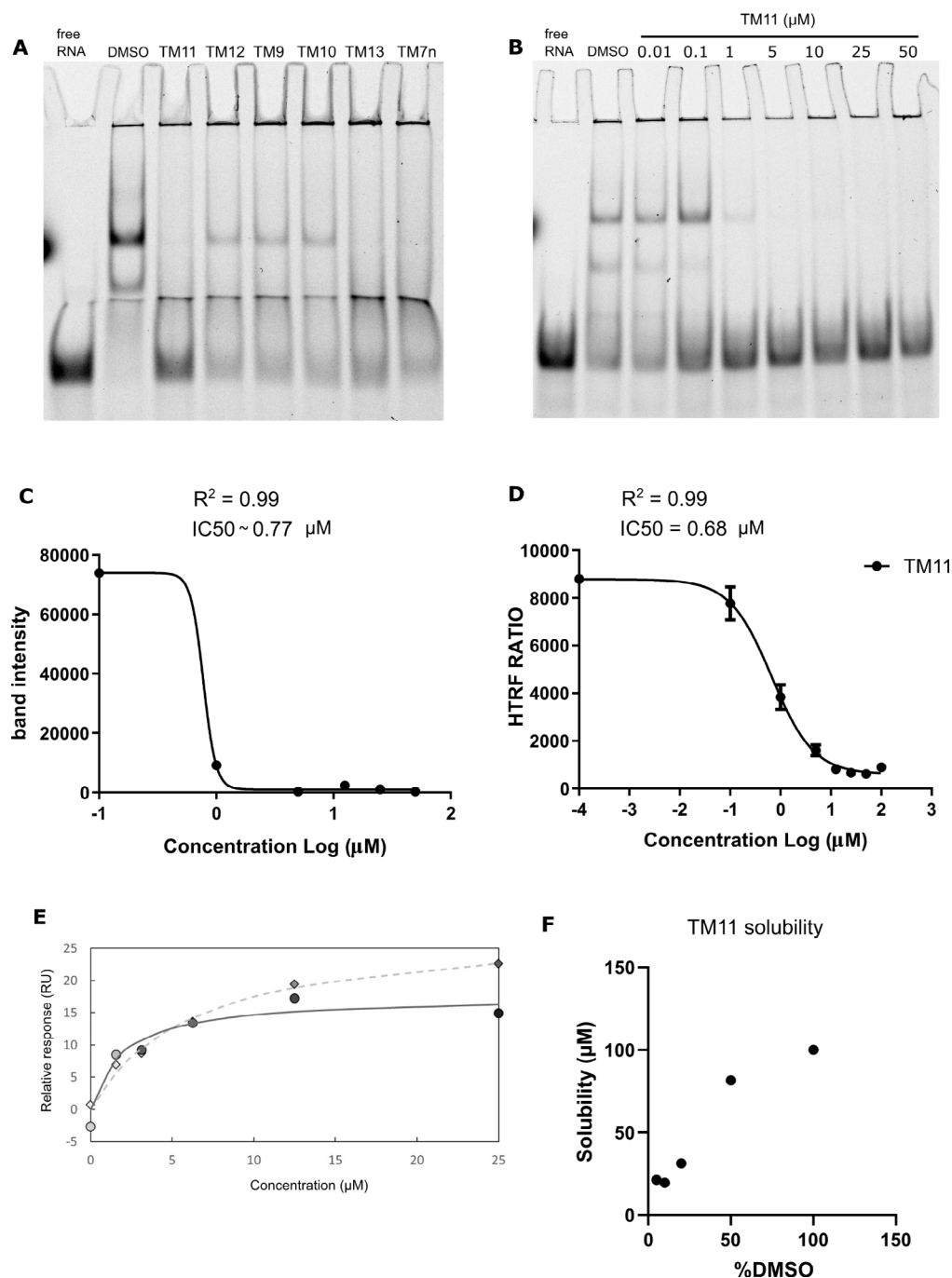
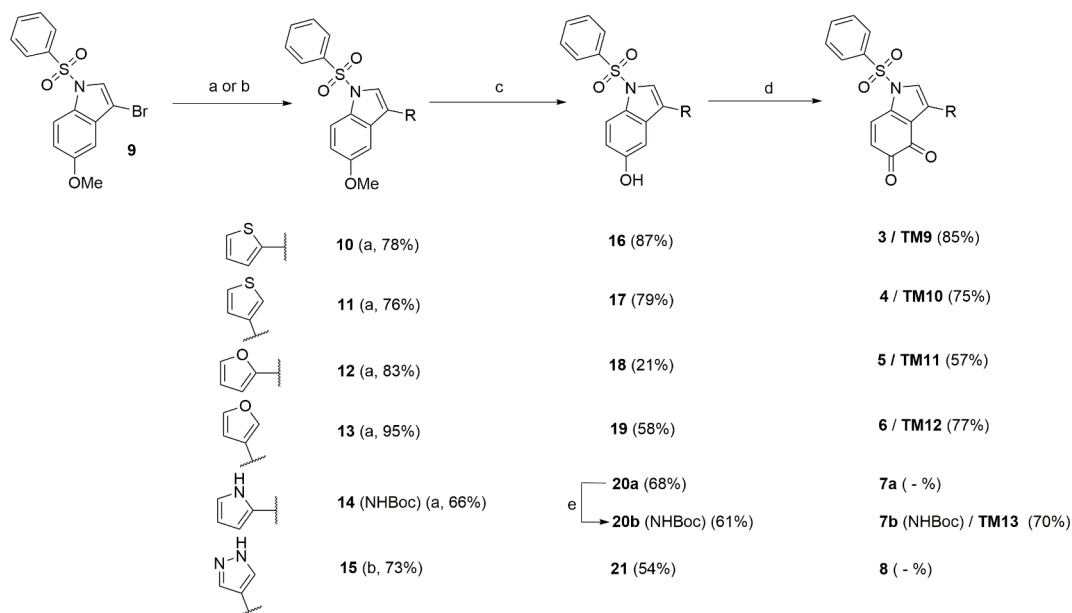


**Fig. 3.** Biochemical and solubility properties of heterocycle-containing tanshinone mimics. **(A)** REMSA screening of TMs. rM1M2\_HuR (3.7 nM) was incubated for 20 min with 1 nM 5'-DY681-labeled RNA probe alone, together with DMSO used as control, or with 2/TM7n, 3-6 and 7b/TM9-13 at 15  $\mu\text{M}$ . The gel was run at 80 V for 100 min. **(B)** Representative REMSA showing 5/TM11 (0.01–25  $\mu\text{M}$ ) dose-response inhibition of the binding between 3.7 nM rM1M2\_HuR and 1 nM 5'-DY681-labeled RNA probe. **(C)** Titration curves of 5/TM11 obtained from REMSA quantification. The calculated half-maximal inhibitory concentration ( $\text{IC}_{50}$ ) is 0.77  $\mu\text{M}$ . **(D)** Dose-response inhibition by 5/TM11 (0.01–100  $\mu\text{M}$ ) of the binding between His-tagged rM1M2 HuR protein (20 nM) and 5'-Bi-TNF ARE probe (50 nM), tested in an HTFR assay. The calculated half-maximal inhibitory concentration ( $\text{IC}_{50}$ ) is 0.68  $\mu\text{M}$ ; data have been normalized to control (DMSO), and fit nonlinear regression fitting curve according to a one-site binding model in GraphPad Prism. Plots are mean  $\pm$  s.d. of three independent experiments. **(E)** Binding of 2/TM7n and 5/TM11 to M1M2 by SPR—representative data from a single measurement. 1:1 binding model fit of steady state responses of 2/TM7n (diamonds, dashed line) and 5/TM11 (circles, full line). **(F)** Solubility of 5/TM11 via LC-MS. The molecule dissolved in DMSO was serially diluted in aqueous medium (phosphate buffer saline, PBS), incubated for 2 h and injected into an LC-MS. Data analysed and plotted with GraphPad Prism as mean  $\pm$  s.d. of two independent experiments.



**Scheme 1.** Synthesis of 3-heteroaryl tanshinone mimics **3–6**, **7b/TM9–13**. (a)  $\text{ArB(OH)}_2$ ,  $\text{Pd(PPh}_3)_4$ , 2 M  $\text{K}_2\text{CO}_3$ , 4:1 DME/EtOH,  $\text{N}_2$ , 100 °C, 8 h, then r.t., 18 h; (b)  $\text{PdCl}_2(\text{dppf})$ , 2 M  $\text{K}_2\text{CO}_3$ , dry dioxane,  $\text{N}_2$ , 100 °C, 8 h, then r.t., 18 h; (c) 1 M  $\text{BBr}_3$  in dry DCM, dry DCM,  $\text{N}_2$ , –78 °C to 0 °C, 3–5 h; (d) IBX, DMF, r.t., 2 h; (e)  $\text{Boc}_2\text{O}$ , DMAP, dry DCM, r.t., 3 h, then piperidine, DCM, r.t., 6 h.

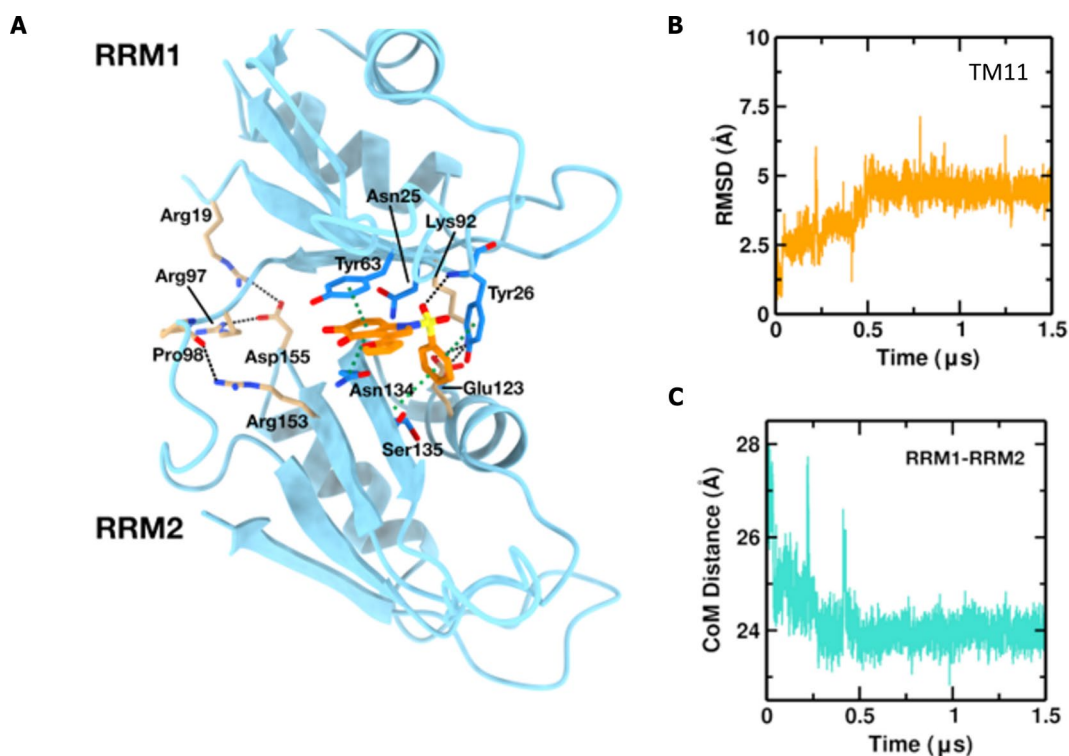


**Fig. 4.** Molecular dynamics calculation of HuR-5/TM11 interactions. (A) Schematic representation of the HuR-5/TM11 complex from MD simulation. 5/TM11 is shown in orange sticks, HuR RRM1-RRM2 domains shown in light blue cartoon representation. HuR residues involved in specific interaction with 5/TM11 and inter-domain interactions are highlighted as turquoise or ochre sticks, respectively. Hydrogens are hidden for clarity. (B) Heavy atoms RMSD along MD simulation of HuR-5/TM11 complex. Prior to RMSD calculations, trajectory was aligned on the Ca of the secondary structural elements with respect to the initial MD frame. (C) RRM1-RRM2 centre of mass distance along MD simulation of HuR-5/TM11 complex. Hydrogens were not included in the centre of mass calculation.



As it regards to Pose A, in the MD average energy-minimized pose, its quinone ring is stacked in a sandwich conformation between Tyr63 (RRM1) and Asn134 (RRM2), establishing a  $\pi$ - $\pi$  and amide- $\pi$  interaction, respectively, and an additional amide- $\pi$  with Asn25 (RRM1) (Fig. 4). The sulfonyl oxygen makes a hydrogen bond with Tyr26 amide backbone (RRM1), while the phenylsulphonyl group is involved in a  $\pi$ - $\pi$  stacking with Tyr26 (RRM1) and an amide- $\pi$  with the backbone of Ser135 (RRM2). These interactions drive the formation of electrostatic contacts between inter-domain residues, further enforcing the closed conformation as shown in Fig. 4.

#### Quantum-mechanics-based simulations

As docking calculations alone were unable to fully explain the binding potency differences observed in REMSAs among 3-heteroaryl TMs 3–6 / TM9–12, and MD requires a long time run for each ligand of interest, quantum-mechanics-based simulations were carried out by Density Functional Theory (DFT, see Materials and Methods for further details). In Fig. 5, the molecular electrostatic potential (MEP) maps for 3–6 / TM9–12 and for the mRNA co-crystallized with HuR (PDB Code: 4ED5) are shown. As expected, their electronic density is largely widespread on the quinone oxygens. However, the electronegative surface becomes larger in furan-containing compounds (5, 6 / TM11, TM12) compared to thiophene-containing ones (3, 4 / TM9, TM10), in agreement with the larger electronegativity of the oxygen atoms compared to sulphur. From DFT calculations, it seems as if 5, 6 / TM11, TM12 better recapitulate the chemical features of RNA bound to HuR (Fig. 5) with respect to 3, 4 / TM9, TM10. Indeed, comparing the electronic density observed for mRNA co-crystallized in HuR complexes (see Fig. 5, left), a similar spatial distribution of electronic density is clearly observed for 5 / TM11. This large, shared region is not observed for 3-furyl isomer 6 / TM12 due to its different oxygen position, located farther from the quinone oxygens and thus incapable of creating a continuous electron-rich surface that, as our results suggest, seems to be a crucial chemical feature for efficient HuR binding. Besides, the oxygen atom of the five-membered ring influences the overall aromaticity degree of the ring. Indeed, furan has been demonstrated to be less aromatic than thiophene both in terms of Diels-Alder reactivity<sup>29</sup> and isotropic magnetic shielding<sup>30</sup>. The larger capability to compromise the HuR-RNA complex by a TM containing a less aromatic ring would be in line with experiments demonstrating a lower capability of HuR to bind to C-rich RNA with respect to U-rich RNA<sup>31</sup>. Indeed, uracil is characterized by a lower aromatic degree in comparison with cytosine<sup>32,33</sup>.

#### Biological activity

##### Cellular effects of 5/TM11 in murine macrophages

To evaluate the potential toxicity of 5 / TM11 on RAW264.7 murine macrophages, we exposed them to increasing concentrations of the compound for 48 h and assessed cell viability using the OZblue viability kit. Our results revealed an  $IC_{50}$  value of 15  $\mu$ M (Fig. 6A), similar to 2 / TM7n<sup>16</sup>. To understand if the decrease of cell number was due to toxic effects or to inhibition of cell proliferation, we performed a cytofluorimetric cell

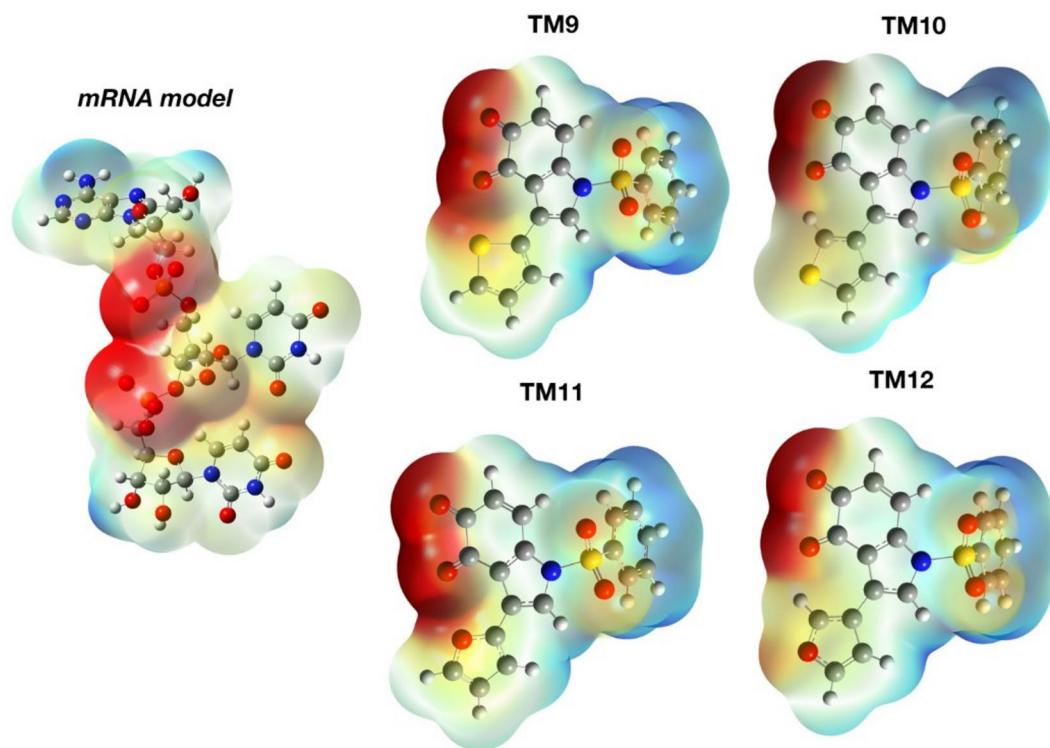


**Fig. 5.** MEPs of the mRNA model (A7, U8, U9) obtained from the mRNA-HuR crystal (PDB Code: 4ED5) and TMs 3–6/TM9–12 calculated at B3LYP/6–31 + G(d, p)-CPCM theory level.

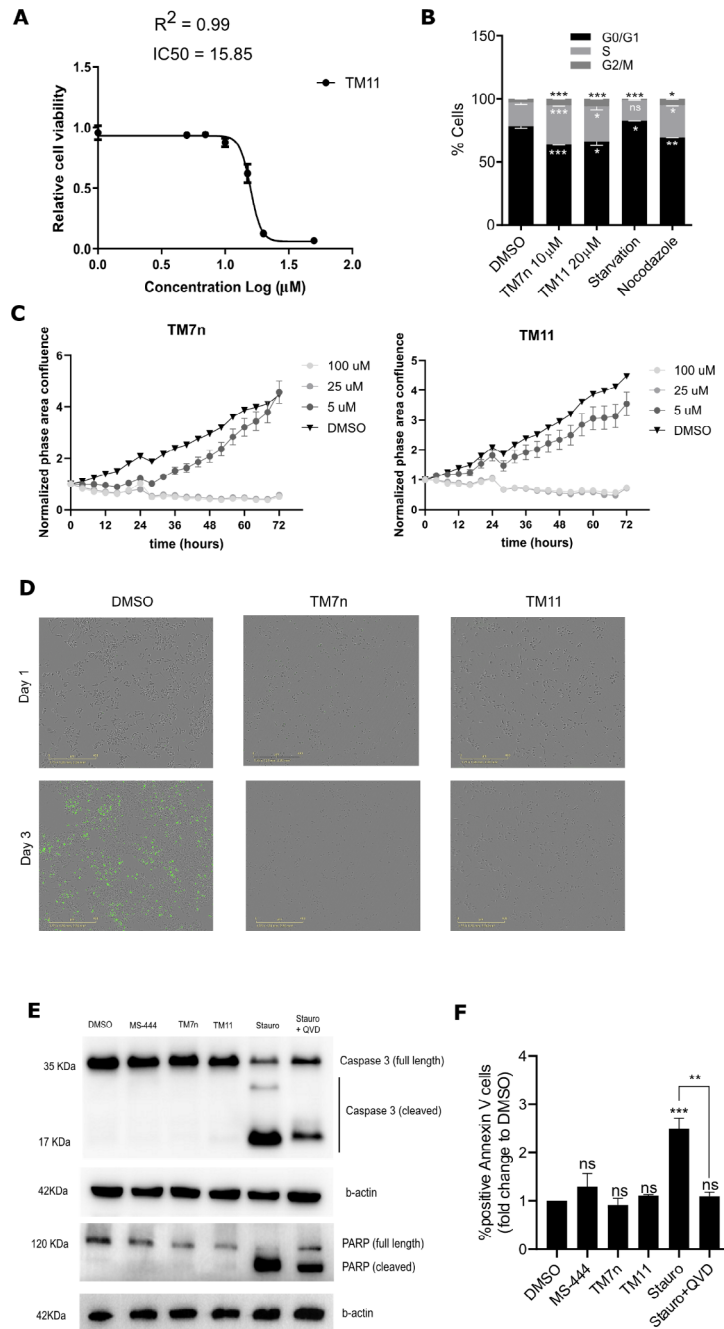


**Fig. 6.** Phenotypic effect of 5/TM11 and 2/TM7n on RAW 264.7 murine macrophages. **(A)** Viability of cells upon treatment with 5/TM11 was assessed via OZ blue viability assay after 48 h of exposure to the compound, ranging from 1 to 50  $\mu\text{M}$ . The calculated  $\text{IC}_{50}$  is identified at 15  $\mu\text{M}$ . Plots are mean  $\pm$  s.d. of three independent experiments. **(B)** Cell cycle analysis of RAW 264.7 cultures upon TMs treatment. Cells were treated with TMs for 48 h and stained with propidium iodide for fluorescence-activated cell sorting (FACS) analysis. Starvation (24 h culturing in serum free media) and nocodazole treatment were used as controls for G0/G1 and G2/M cell cycle blockage. Data analyzed and plotted with GraphPad Prism as mean  $\pm$  s.d. of three independent experiments. **(C)** Growth curve of RAW 264.7 cells upon TMs treatment. Cells were treated with both TMs for 72 h. Data were acquired and analyzed by IncuCyte. Data plotted with GraphPad Prism as mean  $\pm$  s.d. of three independent experiments. **(D)** Activation of Caspase 3/7 in RAW 264.7 cultures upon TMs treatment. Cells were co-treated for 48 h with 2/TM7n or 5/TM11 and the CellEvent™ caspase-3/7 detection reagent. Pictures were acquired every 4 h by IncuCyte. Scale bar 400  $\mu\text{m}$ . Data analyzed and plotted with GraphPad Prism as mean  $\pm$  s.d. of three independent experiments. **(E)** Western blot of activated Caspase 3 and PARP of RAW264.7 cells treated with TMs (15  $\mu\text{M}$ ) and vehicle (DMSO) control for 48 h and with staurosporin (Stauro – 1  $\mu\text{M}$ ) and QVD (10  $\mu\text{M}$ ) for the last 4 h. **(F)** Quantification of the percentage of Annexin V positive cells as a fold change of the control DMSO after the treatment with the TMs and apoptosis controls, in the same conditions as previous. Data was acquired with Symphony A1 and analyzed with BD Diva Software.

cycle analysis using propidium iodide to stain cells' DNA content. Treatment with both **2 / TM7n** and **5 / TM11** at 10  $\mu\text{M}$  and 20  $\mu\text{M}$ , respectively, for 48 h suggested an accumulation of the cells in the S and G2/M phases (Fig. 6B) and a coherent decrease in the G0/G1 phases. We measured cell proliferation by Incucyte, evaluating the real-time growth of cells when exposed to TMs and observed a dose-dependent decrease in proliferation rate in agreement with flow cytometry data (Fig. 6C). This is in line with a previous report indicating that HuR downregulation determines an increase of cells in S and G2/M phases caused by the stabilization of cyclin A and B1 the mRNA in colon cancer cells<sup>34</sup>. Similarly, in B cells, HuR was reported to control the expression of Myc and other genes required for cell cycle entry that led to a decrease in the proliferation rate<sup>35</sup>. However, treatment with the HuR inhibitor CMLD2 on lung cancer cells previously showed a shift towards G1 phase, a trend mirrored in normal cells as well<sup>36</sup>, suggesting that TMs may differ in the mechanism of action when compared to other HuR inhibitors. We further investigated whether the decreased number of viable cells could be ascribed to an apoptotic effect of both TMs, and in comparison, to the reported HuR inhibitor MS-444<sup>22</sup>. We measured the cleavage of caspase 3, by real-time imaging and western blotting, assessed the cleavage of PARP (a molecular target of caspase 3) and evaluated phosphatidylserine exposure on the cell membrane by using Annexin V. We did not observe the activation of the apoptotic machinery, therefore suggesting that both TMs induce a slowdown in RAW cells proliferation rather than apoptosis at the used doses (Fig. 6D–F and Supplementary Fig. S5). The absence of apoptotic effect was shared with MS-444, further validating our observation. Interestingly, the basal level of apoptosis, typically associated with increased cell confluency close to the stationary phase, was not observed during treatments. This is likely because the treated cells, being slowed in proliferation rate, did not reach full confluency at the analyzed time point (Fig. 6D). Based on these findings, we selected a concentration of 10  $\mu\text{M}$ , a dose lower than the  $\text{IC}_{50}$ , for the following experiments with TMs. The aim was to observe the anti-inflammatory activity without causing extensive toxicity.

#### **5/TM11 effect on cytokines expression and release in murine macrophages**

To investigate the impact of **5 / TM11** on the inflammatory response in murine macrophages, we co-treated cells with LPS (1  $\mu\text{g}/\text{mL}$ ) and either **2 / TM7n** and **5 / TM11** (10  $\mu\text{M}$ ), and checked the expression levels of *Cxcl10*, *Fas*, *Nos2* and *Il1 $\beta$*  by qRT-PCR at 6 h post-treatment (Fig. 7A, B). These genes were selected as readout genes of TMs efficacy in this cell model<sup>16</sup>. Consistently, LPS stimulation strongly induced the expression of the readout genes and **5 / TM11** exhibited the ability to counteract the effect of LPS stimulation, similarly to **2 / TM7n**<sup>16</sup>. To further confirm the ability of **5 / TM11** to attenuate LPS-stimulated inflammation, we considered Cxcl10 secretion as a marker of TMs efficacy<sup>16</sup>. We measured Cxcl10 levels by Enzyme Linked Immunosorbent Assay (ELISA) in the supernatant of RAW264.7 cells treated with LPS and **5 / TM11** and observed the downregulation of its level (Fig. 7C). Finally, we administered either **5 / TM11** or **2 / TM7n** 2 h after LPS stimulation to simulate a therapeutic regimen, and measured cytokine expression levels after four hours. A similar decrease in mRNA expression of the selected cytokines and of Cxcl10-secreted protein as in the co-administration regimen (Fig. 7D–F) was observed. Collectively, these results validate the capacity of **5 / TM11** to interfere with the expression of cytokines induced by LPS stimulation, performing similarly to **2 / TM7n**<sup>16</sup> not only when administered concomitantly with LPS<sup>16</sup>, but also in a simulated therapeutic regime when drug administration followed two hours of LPS stimulation. The findings suggest that **5 / TM11** possesses anti-inflammatory properties, as evidenced by its ability to modulate cytokines expression in a similar way as non-heterocyclic TM analogs<sup>16</sup>.

## Conclusion

A novel series of 3-heteroaryl substituted TMs have been synthesized to improve potency and aqueous solubility. From a chemical standpoint, in our previous effort, we introduced ortho substituents on the 3-phenyl ring of the 3-aryl-1,3-TM system to disrupt the ring planarity with the final aim of achieving a major improvement in aqueous solubility<sup>16</sup>. However, our results were still sub-optimal both for in-cellular and in vivo tests. Herein, we report the synthesis of a new class of TMs where the 3-phenyl ring of early lead **TM6a** was replaced with an array of polar 5-membered heterocycles. Among them, 3-(2-furyl) **5 / TM11** resulted in being an order of magnitude more soluble than earlier leads **1 / TM6a** and **2 / TM7n**, while also as potent as **2 / TM7n** as a HuR inhibitor, as measured by SPR. MD simulations clearly indicate that **5 / TM11** drives the closure of RRM domains, resembling the effect of endogenous ligand mRNAs<sup>14</sup>. Quantomechanical calculations suggest that the higher binding affinity showed by 3-furan- vs. 3-thiophene-substituted TMs is due to their better mimicking of RNA molecules both in terms of charge distribution and ring aromaticity. Finally, we characterized the activity of **5 / TM11** on macrophages, identifying a dose that induces proliferation slowdown without causing apoptosis, and evaluating its ability to counteract the expression of proinflammatory genes induced by LPS stimulation. In this regard, **5 / TM11** is a novel member of TMs endowed with better aqueous solubility, slightly higher potency and with similar anti-inflammatory mechanism of action of the previously described TMs<sup>16</sup>. HuR is one of the most studied RBP in the immune system, due to its well-established involvement in the inflammatory response. Indeed, HuR pro-inflammatory role is widely demonstrated, exemplified by the inverse correlation between the anti-inflammatory cytokine IL10 and HuR levels<sup>37</sup>. Notably, HuR has also been implicated in promoting LPS-endothelial injury<sup>38</sup>. However, other studies have reported how HuR expression had a protective role against inflammation<sup>11,39</sup>, with its role remaining controversial<sup>40</sup>. This dichotomy underlines the intricate and context-dependent behavior of HuR within the immune system. Further exploration is required to unravel how HuR modulation may affect inflammatory response in therapeutic conditions; to this regard, our study suggests that the furan substitution in TM scaffold maintains the main properties of the class but shows improved biochemical properties.



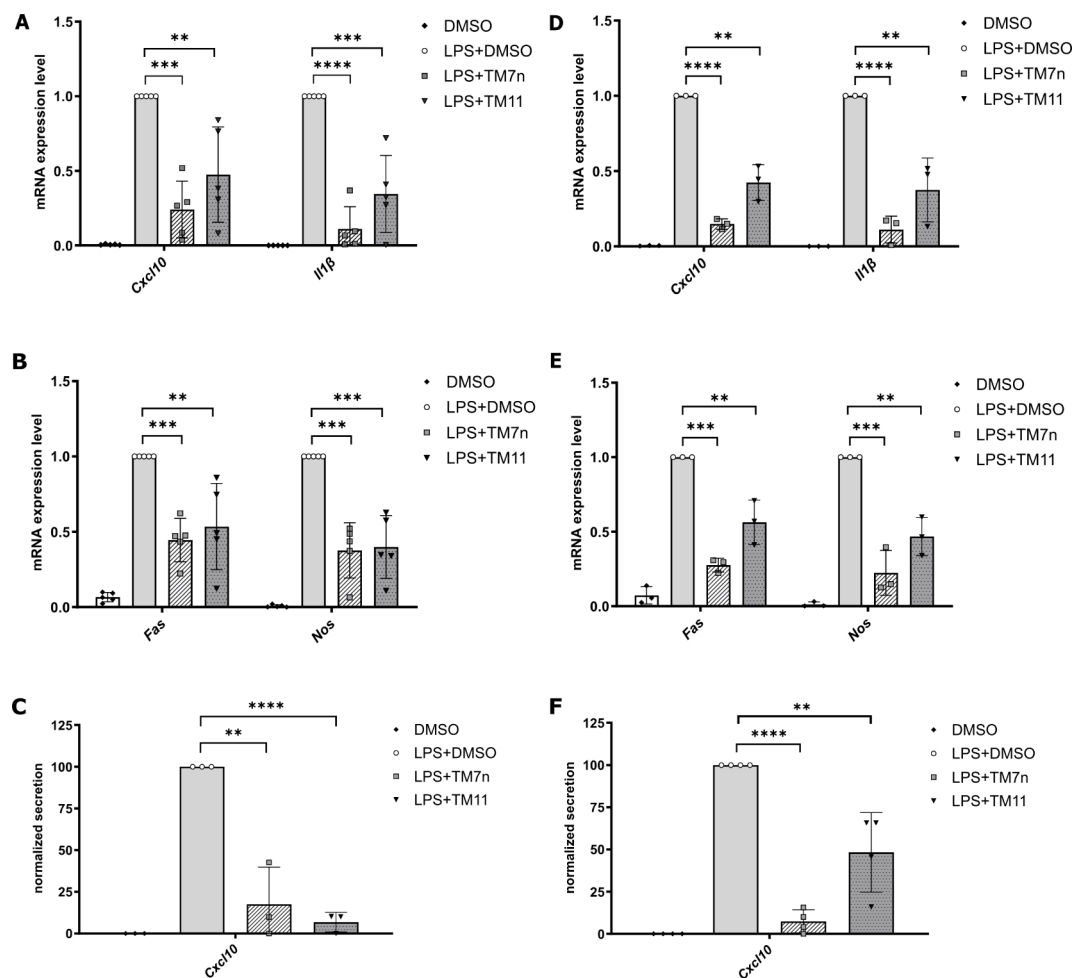


**Fig. 7.** 5/TM11 effect on cytokines expression and release in murine macrophages. (**A, B**) Expression of cytokines in treated RAW264.7 cultures. Cells were co-treated for 6 h with LPS (1  $\mu\text{g}/\text{mL}$ ) and 2/TM7n, 5/TM11 (10  $\mu\text{M}$ ) or DMSO as control. Expression levels were assessed via qRT-PCR, using RPLP0 as housekeeping gene. Data were normalized to LPS + DMSO condition. Data analysed and plotted with GraphPad Prism as mean  $\pm$  s.d. of at least three independent experiments. (**C**) Secretion of cxcl10 in RAW264.7. Cxcl10 secretion was measured via ELISA on RAW264.7 supernatant. Cells were co-treated for 6 h with LPS (1  $\mu\text{g}/\text{mL}$ ) and 2/TM7n, 5/TM11 (10  $\mu\text{M}$ ) or DMSO as control. The relative quantity of Cxcl10 pg/mL for each sample was normalized according to the number of cells quantified through Crystal Violet assay. Data were normalized to LPS + DMSO as control, and numbers are expressed as a percentage. Data analysed and plotted with GraphPad Prism as mean  $\pm$  s.d. of three independent experiments. (**D, E**) Expression of cytokines in treated RAW264.7 cultures. Cells were stimulated for 2 h with LPS (1  $\mu\text{g}/\text{mL}$ ) and subsequently treated with 2/TM7n, 5/TM11 (10  $\mu\text{M}$ ) or DMSO as control for 4 h. Expression levels were assessed via qRT-PCR, using RPLP0 as a housekeeping gene. Data were normalized to LPS + DMSO condition. Data analysed and plotted with GraphPad Prism as mean  $\pm$  s.d. of at least three independent experiments. (**F**) Secretion of cxcl10 in RAW264.7 cells. Cxcl10 secretion was measured via ELISA on RAW264.7 supernatant. Cells were stimulated for 2 h with LPS (1  $\mu\text{g}/\text{mL}$ ) and subsequently treated with 2/TM7n, 5/TM11 (10  $\mu\text{M}$ ) or DMSO. The relative quantity of Cxcl10 pg/mL for each sample was normalized according to the number of cells quantified through Crystal Violet assay. Data were normalized to LPS + DMSO as control, and numbers are expressed as a percentage. Data analysed and plotted with GraphPad Prism as mean  $\pm$  s.d. of three independent experiments.

## Materials and methods

### General methods for chemistry

Reagent-grade chemicals and solvents were purchased from Sigma-Aldrich or FluoroChem, and were used without any further purification. Dry solvents were purchased from Sigma-Aldrich, and reactions in anhydrous conditions were performed under nitrogen atmosphere, using a dry nitrogen flux (passage through Drierite ( $\text{Ca}_2\text{SO}_4$ ) traps as a drying agent). Reactions were monitored by analytical thin-layer chromatography (TLC) using silica gel 60 F254 pre-coated glass plates (0.25 mm thickness). Visualization was accomplished by irradiation with a UV lamp and/or staining with cerium/molybdate reagent. Purifications were carried out either by direct phase flash chromatography on Macherey-Nagel silica gel (particle size 60  $\mu\text{m}$ , 230–400 mesh), or

through an automated Biotage™ chromatography system. NMR spectra were recorded on a Bruker Advance 400 instrument in deuterated solvents either at 400 MHz (<sup>1</sup>H-NMR) or at 101 MHz (<sup>13</sup>C NMR spectra). Chemical shifts are expressed in δ - ppm with the solvent reference relative to tetramethylsilane (TMS) employed as an internal standard. Coupling constants are given in Hertz and rounded to the nearest 0.1 Hz. The following abbreviations are used to describe spin multiplicity: s = singlet, d = doublet, t = triplet, q = quartet, m = multiplet, bs = broad signal, dd = doublet of doublets, ddd = doublet of doublets of doublets, ddt = doublet of doublets of triplets, td = triplet of doublets. LC-MS data were collected with a Waters Acquity Ultra performance LC (UPLC)-MS System equipped with a TUV detector, a single quadrupole SQD mass spectrometer and ACQUITY UPLC BEH SHIELD RP<sub>18</sub> columns (2.1 × 100 mm, id = 1.7 μm). HPLC compounds' purity was determined by monitoring at 220 nm using H<sub>2</sub>O (HiPerSolv Chromanorm Water VWR for HPLC-MS) + 0.05% trifluoroacetic acid (spectroscopic grade) (phase A) and acetonitrile (HiPerSolv Chromanorm Acetonitrile SuperGradient VWR) + 0.05% trifluoroacetic acid (spectroscopic grade) (phase B), and a gradient from 5% B to 100% B in 5 min, followed by 100% B for 1 min; a 0.5 mL/min flow was used, with 2 min equilibration time.

### General procedure A: Suzuki coupling

In a two-necked round-bottom flask, equipped with a valve on the lateral neck and with a rubber septum on the main-middle neck, 3-bromo-5-methoxy-1-(phenylsulfonyl)-1 H-indole **9** (1.0 eq) and the corresponding boronic acid (1.17 eq) were added, then the flask was flushed with nitrogen to remove any trace of oxygen. Subsequently, dry and previously deaerated 4:1 DME/EtOH and a 2 M aqueous K<sub>2</sub>CO<sub>3</sub> solution (1.29 eq) were added. Finally, Pd(PPh<sub>3</sub>)<sub>4</sub> (0.05 eq) was added under nitrogen flushing. The rubber septum was removed, and a condenser equipped with a valve was fitted onto the main-middle neck. The solution was stirred under N<sub>2</sub> at reflux (100 °C) for 8 h, then at room temperature for additional 12 h, monitoring by TLC (eluent mixture: 7:3 n-hexane/EtOAc, developed in molybdic reagent). Finally, the reaction was diluted with a saturated NH<sub>4</sub>Cl solution and extracted thrice with EtOAc. The collected organic phases were washed with brine, dried over sodium sulfate, filtered and the solvent was evaporated under reduced pressure. The crude was purified by flash chromatography.

#### Synthesis of 5-methoxy-1-(phenylsulfonyl)-3-(thiophen-2-yl)-1 H-indole **10**

Intermediate **10** was synthesized according to general procedure A, starting from 3-bromo-5-methoxy-1-(phenylsulfonyl)-1 H-indole **9** (200 mg, 0.55 mmol, 1 eq), 2-thiophen-boronic acid (81.9 mg, 0.64 mmol, 1.17 eq) and Pd(PPh<sub>3</sub>)<sub>4</sub> (31.8 mg, 0.028 mmol, 0.05 eq) in 4:1 dry degassed DME/EtOH (9.8 mL). The crude was purified by flash chromatography (eluent mixture: 8:2 n-hexane/EtOAc), yielding 159.3 mg of pure compound **10** as a white solid (0.431 mmol, 78% yield). MS (ESI<sup>+</sup>): m/z 370.07 [M + H]<sup>+</sup>. Calculated MS for C<sub>19</sub>H<sub>15</sub>NO<sub>3</sub>S<sub>2</sub>: 369.05. <sup>1</sup>H NMR (400 MHz, acetone-d<sub>6</sub>) δ (ppm): 8.07–8.02 (m, 2 H, CH phenyl-sulfonamide), 7.99 (d, J = 9.0 Hz, 1 H, H7 indole), 7.94 (s, 1 H, H2 indole), 7.73–7.64 (m, 1 H, CH phenyl-sulfonamide), 7.64–7.55 (m, 2 H, CH phenyl-sulfonamide), 7.55–7.49 (m, 2 H, CH thiophene), 7.36 (d, J = 2.5 Hz, 1 H, H4 indole), 7.22–7.15 (m, 1 H, CH thiophene), 7.05 (dd, J = 9.2, 2.5 Hz, 1 H, H6 indole), 3.85 (s, 3 H, OCH<sub>3</sub>). <sup>13</sup>C NMR (101 MHz, acetone-d<sub>6</sub>) δ (ppm): 158.2, 138.7, 135.3, 130.5, 128.8, 127.8, 126.0, 125.7, 124.5, 118.6, 115.7, 115.2, 103.8, 56.0.

#### Synthesis of 5-methoxy-1-(phenylsulfonyl)-3-(thiophen-3-yl)-1 H-indole **11**

Intermediate **11** was synthesized according to general procedure A, starting from 3-bromo-5-methoxy-1-(phenylsulfonyl)-1H-indole **9** (200 mg, 0.55 mmol, 1 eq), 3-thiophen-boronic acid (81.9 mg, 0.64 mmol, 1.17 eq) and Pd(PPh<sub>3</sub>)<sub>4</sub> (31.8 mg, 0.028 mmol, 0.05 eq) in 4:1 dry, degassed DME/EtOH (9.8 mL). The crude was purified by flash chromatography (eluent mixture: gradient from 8:2 to 6:4 n-hexane/EtOAc), yielding 152.6 mg of pure compound **11** as a white solid (0.413 mmol, 76% yield). MS (ESI<sup>+</sup>): m/z 370.33 [M + H]<sup>+</sup>. Calculated MS for C<sub>19</sub>H<sub>15</sub>NO<sub>3</sub>S<sub>2</sub>: 369.05. <sup>1</sup>H NMR (400 MHz, acetone-d<sub>6</sub>) δ (ppm): 8.06–8.00 (m, 2 H, CH phenyl-sulfonamide), 7.98 (dd, J = 9.1, 0.5 Hz, 1H, H7 indole), 7.95 (s, 1H, H2 indole), 7.84 (dd, J = 2.9, 1.4 Hz, 1H, CH thiophene), 7.70–7.63 (m, 1H, CH phenyl-sulfonamide), 7.63–7.54 (m, 4 H, CH phenyl-sulfonamide, CH thiophene), 7.35 (d, J = 2.5 Hz, 1H, H4 indole), 7.03 (dd, J = 9.1, 2.5 Hz, 1H, H6 indole), 3.85 (s, 3 H, OCH<sub>3</sub>). <sup>13</sup>C NMR (101 MHz, acetone-d<sub>6</sub>) δ (ppm): 157.3, 138.8, 135.1, 134.2, 131.1, 130.9, 130.4, 128.1, 127.8, 127.2, 125.0, 122.3, 120.7, 115.6, 114.9, 104.0, 56.0.

#### Synthesis of 3-(furan-2-yl)-5-methoxy-1-(phenylsulfonyl)-1 H-indole **12**

Intermediate **12** was synthesized according to general procedure A, starting from 3-bromo-5-methoxy-1-(phenylsulfonyl)-1H-indole **9** (887.6 mg, 2.424 mmol, 1 eq), 2-furan-boronic acid (317.3 mg, 2.836 mmol, 1.17 eq) and Pd(PPh<sub>3</sub>)<sub>4</sub> (140.0 mg, 0.121 mmol, 0.05 eq) in 4:1 dry, degassed DME/EtOH (43 mL). The crude was purified by flash chromatography (eluent mixture: 7:3 n-hexane/EtOAc), yielding 709.0 mg of pure compound **12** as a white solid (2.012 mmol, 83% yield). MS (ESI<sup>+</sup>): m/z 354.24 [M + H]<sup>+</sup>. Calculated MS for C<sub>19</sub>H<sub>15</sub>NO<sub>4</sub>S: 353.07. <sup>1</sup>H NMR (400 MHz, acetone-d<sub>6</sub>) δ (ppm): 8.05–8.01 (m, 2 H), 8.00–7.95 (m, 2 H, H7 indole, H2 indole), 7.70–7.64 (m, 2 H, CH phenyl-sulfonamide, CH furan), 7.62–7.54 (m, 2 H, CH phenyl-sulfonamide), 7.41 (d, J = 2.5 Hz, 1H, H4 indole), 7.04 (dd, J = 9.1, 2.5 Hz, 1H, H6 indole), 6.91 (dd, J = 3.4, 0.7 Hz, 1H, CH furan), 6.59 (dd, J = 3.4, 1.9 Hz, 1H, CH furan), 3.86 (s, 3 H, OCH<sub>3</sub>). <sup>13</sup>C NMR (101 MHz, acetone-d<sub>6</sub>) δ (ppm) 158.1, 148.8, 142.9, 138.6, 135.2, 130.5, 129.3, 127.8, 123.6, 115.5, 115.2, 107.6, 104.3, 56.0.

#### Synthesis of 5-methoxy-1-(phenylsulfonyl)-3-(furan-3-yl)-1 H-indole **13**

Intermediate **13** was synthesized according to general procedure A, starting from 3-bromo-5-methoxy-1-(phenylsulfonyl)-1H-indole **9** (300 mg, 0.819 mmol, 1 eq), 3-furan-boronic acid (107.2 mg, 0.958 mmol, 1.17 eq) and Pd(PPh<sub>3</sub>)<sub>4</sub> (47.3 mg, 0.041 mmol, 0.05 eq) in 1:4 dry EtOH/DME (14.6 mL). The crude was purified by flash chromatography (eluent mixture: 7:3 n-hexane/EtOAc), yielding 288.0 mg of pure compound **13** as a white solid

(0.815 mmol, 99% yield). MS (ESI<sup>+</sup>): m/z 354.00 [M + H]<sup>+</sup>. Calculated MS for C<sub>19</sub>H<sub>15</sub>NO<sub>4</sub>S: 353.07. <sup>1</sup>H NMR (400 MHz, acetone-d<sub>6</sub>) δ (ppm): 8.16 (s, 1H, CH furan), 8.01–7.96 (m, 3 H, H7 indole, CH phenyl-sulfonamide), 7.92 (s, 1H, H2 indole), 7.70–7.64 (m, 2 H, CH furan, CH phenyl-sulfonamide), 7.59–7.54 (m, 2 H, CH phenyl-sulfonamide), 7.24 (d, J = 2.5 Hz, 1H, H4 indole), 7.02 (dd, J = 9.0, 2.5 Hz, 1H, H6 indole), 6.98 (dd, J = 1.9, 1.2 Hz, 1H, CH furan), 3.86 (s, 3 H, OCH<sub>3</sub>). <sup>13</sup>C NMR (101 MHz, acetone-d<sub>6</sub>) δ (ppm): 158.1, 144.5, 140.4, 138.8, 135.1, 130.9, 130.4, 127.7, 124.7, 118.7, 116.6, 115.6, 114.9, 110.5, 104.1, 56.0.

#### Synthesis of tert-butyl 2-(5-methoxy-1-(phenylsulfonyl)-1H-indol-3-yl)-1H-pyrrole-1-carboxylate **14**

Intermediate **14** was synthesized according to general procedure A, starting from 3-bromo-5-methoxy-1-(phenylsulfonyl)-1H-indole **9** (300.0 mg, 0.819 mmol, 1 eq), (1-(Boc)-1H-pyrrol-2-yl)boronic acid (202.2 mg, 0.958 mmol, 1.17 eq) and Pd(PPh<sub>3</sub>)<sub>4</sub> (47.3 mg, 0.041 mmol, 0.05 eq) in 4:1 dry, degassed DME/EtOH (14.6 mL). The crude was purified by flash chromatography (eluent mixture: 8:2 n-hexane/EtOAc), yielding 245 mg of pure compound **14** as a white solid (0.540 mmol, 66% yield). MS (ESI<sup>+</sup>): m/z 453.27 [M + H]<sup>+</sup>. Calculated MS for C<sub>24</sub>H<sub>24</sub>N<sub>2</sub>O<sub>5</sub>S: 452.14. <sup>1</sup>H NMR (400 MHz, acetone-d<sub>6</sub>) δ (ppm): 8.11–8.03 (m, 2 H, CH phenyl-sulfonamide), 7.96 (d, J = 9.1 Hz, 1H, H7 indole), 7.73–7.64 (m, 2 H, H2 indole, CH phenyl-sulfonamide), 7.64–7.53 (m, 2 H, CH phenyl-sulfonamide), 7.46 (dd, J = 3.3, 1.9 Hz, 1H, CH pyrrole), 6.99 (dd, J = 9.0, 2.5 Hz, 1H, H6 indole), 6.83 (d, J = 2.5 Hz, 1H, H4 indole), 6.36–6.28 (m, 2 H, CH pyrrole), 3.76 (s, 3 H, OCH<sub>3</sub>), 0.97 (s, 9 H, Boc). <sup>13</sup>C NMR (101 MHz, acetone-d<sub>6</sub>) δ (ppm): 157.7, 139.0, 135.1, 133.5, 130.5, 130.0, 127.9, 126.1, 125.6, 123.9, 118.9, 116.5, 115.3, 114.8, 111.6, 104.0, 84.3, 55.9, 27.2.

#### Synthesis of 5-methoxy-1-(phenylsulfonyl)-3-(1H-pyrazol-4-yl)-1H-indole **15**

In a two-necked round-bottom flask, equipped with a valve on the lateral neck and with a rubber septum on the main-middle neck, bromo-methoxyindole **9** (50.0 mg, 0.137 mmol, 1 eq) and 4-pyrazoleboronic acid pinacol ester (31.1 mg, 0.160 mmol, 1.17 eq) were added, then the flask was flushed with nitrogen to remove any trace of oxygen. Subsequently, dry and previously deaired dioxane (0.60 mL) and a 2 M aqueous K<sub>2</sub>CO<sub>3</sub> solution (0.23 mL, 0.456 mmol, 3.33 eq) were added. Finally, PdCl<sub>2</sub>(dppf) (10.0 mg, 0.014 mmol, 0.1 eq) was added under nitrogen flushing. The rubber septum was removed, and a condenser equipped with a valve was fitted onto the main-middle neck. The solution was stirred under N<sub>2</sub> at reflux (100 °C) for 7 h, then at room temperature for additional 12 h, monitoring by TLC (eluent mixture: 7:3 n-hexane/EtOAc, developed in molybdc reagent). Finally, the reaction was diluted with a saturated NH<sub>4</sub>Cl solution (2 mL) and extracted with EtOAc (3 × 5 mL). The collected organic phases were washed with brine, dried over sodium sulfate, filtered and the solvent was evaporated under reduced pressure. The crude was purified by flash chromatography (eluent mixture: 7:3 n-hexane/EtOAc), yielding 35.3 mg of pure compound **15** as white solid (0.099 mmol, 73% yield). MS (ESI<sup>+</sup>): m/z 354.04 [M + H]<sup>+</sup>. Calculated MS for C<sub>18</sub>H<sub>15</sub>N<sub>3</sub>O<sub>3</sub>S: 353.08. <sup>1</sup>H NMR (400 MHz, acetone-d<sub>6</sub>) δ (ppm): 7.97–7.94 (m, 2 H, CH phenyl-sulfonamide), 7.90 (dt, J = 9.1, 0.7 Hz, 1H, H7 indole), 7.71–7.62 (m, 3 H, H2 indole, CH phenyl-sulfonamide, CH pyrazole), 7.62–7.52 (m, 2 H, CH phenyl-sulfonamide), 7.08 (d, J = 2.5 Hz, 1H, H4 indole), 6.94 (dd, J = 9.0, 2.6 Hz, 1H, H6 indole), 6.72 (dd, J = 3.7, 0.8 Hz, 1H, CH pyrazole), 3.79 (s, 2 H, OCH<sub>3</sub>). <sup>13</sup>C NMR (101 MHz, acetone-d<sub>6</sub>) δ (ppm): 157.7, 139.0, 135.0, 133.0, 130.4, 128.3, 127.6, 115.1, 114.6, 110.5, 104.6, 55.8.

#### General procedure B: removal of methoxy group

A 1 M solution of BBr<sub>3</sub> in dry DCM (6 eq) was slowly added under stirring to a solution of methoxyindoles **10–15** (1 eq) in dry DCM (0.1 M), under nitrogen atmosphere and at -78 °C. The temperature was slowly increased to 0 °C while monitoring the reaction by TLC (eluent mixture: 7:3 n-hexane/EtOAc, developed in molybdc reagent). After reaction completion (3–5 h), still at 0 °C, the solution was diluted with distilled water and neutralized with a saturated NaHCO<sub>3</sub> solution. The reaction mixture was extracted three times with DCM the collected organic layers were washed with brine, dried over sodium sulfate, and filtered. The solvent was removed under reduced pressure and the crude was purified by flash chromatography.

#### Synthesis of 1-(phenylsulfonyl)-3-(thiophen-2-yl)-1H-indol-5-ol **16**

Compound **14** was synthesized according to general procedure B, starting from intermediate **10** (147.8 mg, 0.400 mmol, 1 eq) and 1 M BBr<sub>3</sub> (2.4 mL) in dry DCM (4.0 mL). The crude was purified by column chromatography (eluent mixture: 7:3 n-hexane/EtOAc), affording 123.5 mg of pure compound **16** as a yellow solid (0.347 mmol, 87% yield). MS (ESI<sup>+</sup>): m/z 356.24 [M + H]<sup>+</sup>. Calculated MS for C<sub>18</sub>H<sub>13</sub>NO<sub>3</sub>S<sub>2</sub>: 355.03. <sup>1</sup>H NMR (400 MHz, acetone-d<sub>6</sub>) δ (ppm): 8.43 (s, 1H, OH), 8.07–8.00 (m, 2 H, CH phenyl-sulfonamide), 7.97–7.89 (m, 2 H, H2 indole, H7 indole), 7.72–7.63 (m, 1H, CH phenyl-sulfonamide), 7.63–7.54 (m, 2 H, CH phenyl-sulfonamide), 7.50 (dd, J = 5.1, 1.1 Hz, 1H, CH thiophene), 7.46 (dd, J = 3.6, 1.1 Hz, 1H, CH thiophene), 7.33 (d, J = 2.4 Hz, 1H, H4 indole), 7.17 (dd, J = 5.1, 3.6 Hz, 1H, CH thiophene), 6.98 (dd, J = 8.9, 2.4 Hz, 1H, H6 indole). <sup>13</sup>C NMR (101 MHz, acetone-d<sub>6</sub>) δ (ppm): 155.6, 138.7, 135.3, 135.2, 130.9, 130.5, 130.3, 128.6, 127.82, 125.7, 125.5, 124.4, 118.4, 115.6, 115.4, 115.3, 106.2, 106.1.

#### Synthesis of 1-(phenylsulfonyl)-3-(thiophen-3-yl)-1H-indol-5-ol **17**

Compound **17** was synthesized according to general procedure B, starting from intermediate **11** (140.3 mg, 0.380 mmol, 1 eq) and 1 M BBr<sub>3</sub> (2.3 mL) in dry DCM (3.8 mL). The crude was purified by column chromatography (eluent mixture: 6:4 n-hexane/EtOAc), affording 105.6 mg of pure compound **17** as a white solid (0.30 mmol, 79% yield). MS (ESI<sup>+</sup>): m/z 356.04 [M + H]<sup>+</sup>. Calculated MS for C<sub>18</sub>H<sub>13</sub>NO<sub>3</sub>S<sub>2</sub>: 355.03. <sup>1</sup>H NMR (400 MHz, acetone-d<sub>6</sub>) δ (ppm): 8.33 (s, 1H, OH), 8.06–7.98 (m, 2 H, CH phenyl-sulfonamide), 7.92–7.90 (m, 2 H, H2 indole, H7 indole), 7.74 (dd, J = 2.9, 1.3 Hz, 1H, CH thiophene), 7.69–7.63 (m, 1H, CH phenyl-sulfonamide), 7.63–7.51 (m, 4 H, CH phenyl-sulfonamide, CH thiophene), 7.28 (d, J = 2.4 Hz, 1H, H4 indole), 6.96 (dd, J = 8.9,

2.5 Hz, 1H, H6 indole).  $^{13}\text{C}$  NMR (101 MHz, acetone- $d_6$ )  $\delta$  (ppm) 155.5, 138.8, 135.0, 134.4, 131.4, 130.4, 128.0, 127.8, 127.1, 124.9, 122.0, 120.0, 115.6, 115.0, 106.3.

#### Synthesis of 3-(furan-2-yl)-1-(phenylsulfonyl)-1 H-indol-5-ol **18**

Compound **18** was synthesized according to general procedure B, starting from intermediate **12** (408.7 mg, 1.565 mmol, 1 eq) and 1 M  $\text{BBr}_3$  (6.9 mL) in dry DCM (15.6 mL). The crude was purified by column chromatography (eluent mixture: 7:3 n-hexane/EtOAc), affording 111.5 mg of pure compound **18** as a brown solid (0.329 mmol, 21% yield). MS (ESI $^+$ ):  $m/z$  340.22  $[\text{M} + \text{H}]^+$ . Calculated MS for  $\text{C}_{18}\text{H}_{13}\text{NO}_4\text{S}$ : 339.06.  $^1\text{H}$  NMR (400 MHz, acetone- $d_6$ )  $\delta$  (ppm): 8.40 (s, 1H, OH), 8.03–8.00 (m, 2 H, CH phenyl-sulfonamide), 7.92–7.89 (m, 2 H, H2 indole, H7 indole), 7.71–7.62 (m, 2 H, CH phenyl-sulfonamide, CH furan), 7.62–7.53 (m, 2 H, CH phenyl-sulfonamide), 7.36 (d,  $J = 2.4$  Hz, 1H, H4 indole), 6.97 (dd,  $J = 9.0, 2.4$  Hz, 1H, H6 indole), 6.81 (d,  $J = 3.3$  Hz, 1H, CH furan), 6.58 (dd,  $J = 3.4, 1.9$  Hz, 1H, CH furan).  $^{13}\text{C}$  NMR (101 MHz, acetone- $d_6$ )  $\delta$  (ppm): 155.5, 142.8, 135.2, 130.5, 129.2, 127.8, 125.0, 123.5, 115.5, 115.4, 112.3, 107.3, 106.7.

#### Synthesis of 3-(furan-3-yl)-1-(phenylsulfonyl)-1 H-indol-5-ol **19**

Compound **19** was synthesized according to general procedure B, starting from intermediate **13** (216.4 mg, 0.612 mmol, 1 eq) and 1 M  $\text{BBr}_3$  (3.7 mL) in dry DCM (6.1 mL). The crude was purified by column chromatography (eluent mixture: 6:4 n-hexane/EtOAc), affording 121.3 mg of pure compound **19** as a brown solid (0.357 mmol, 58% yield). MS (ESI $^+$ ):  $m/z$  340.16  $[\text{M} + \text{H}]^+$ . Calculated MS for  $\text{C}_{18}\text{H}_{13}\text{NO}_4\text{S}$ : 339.06.  $^1\text{H}$  NMR (400 MHz, acetone- $d_6$ )  $\delta$  (ppm): 8.38 (s, 1H, OH), 8.04–8.01 (m, 1H, CH furan), 8.02–7.95 (m, 2 H, CH phenyl-sulfonamide), 7.90 (d,  $J = 8.9$  Hz, 1H, H7 indole), 7.88 (s, 1H, H2 indole), 7.69–7.61 (m, 2 H, CH furan, CH phenyl-sulfonamide), 7.60–7.52 (m, 2 H, CH phenyl-sulfonamide), 7.16 (d,  $J = 2.4$  Hz, 1H, H4 indole), 6.99–6.91 (m, 2 H, H6 indole, CH furan).  $^{13}\text{C}$  NMR (101 MHz, acetone- $d_6$ )  $\delta$  (ppm): 155.4, 144.5, 140.1, 138.8, 135.0, 131.3, 130.4, 127.7, 124.6, 118.9, 116.4, 115.5, 115.0, 114.9, 110.4, 106.4.

#### Synthesis of 1-(phenylsulfonyl)-3-(1 H-pyrrol-2-yl)-1 H-indol-5-ol **20a**

Compound **20a** was synthesized according to general procedure B, starting from intermediate **14** (245 mg, 0.540 mmol, 1 eq) and 1 M  $\text{BBr}_3$  (3.2 mL) in dry DCM (5.4 mL). The crude was purified by column chromatography (eluent mixture: 6:4 n-hexane/EtOAc), affording 160.7 mg of pure compound **20a** as a white solid (0.475 mmol, 88% yield). MS (ESI $^+$ ):  $m/z$  339.21  $[\text{M} + \text{H}]^+$ . Calculated MS for  $\text{C}_{18}\text{H}_{14}\text{N}_2\text{O}_3\text{S}$ : 338.07.  $^1\text{H}$  NMR (400 MHz, acetone- $d_6$ )  $\delta$  (ppm): 10.48 (bs, 1H, NH), 8.31 (bs, 1H, OH), 8.00–7.91 (m, 2 H, CH phenyl-sulfonamide), 7.88 (d,  $J = 8.9$  Hz, 1H, H7 indole), 7.83 (s, 1H, H2 indole), 7.68–7.60 (m, 1H, CH phenyl-sulfonamide), 7.60–7.50 (m, 2 H, CH phenyl-sulfonamide), 7.30 (d,  $J = 2.3$  Hz, 1H, H4 indole), 6.94 (dd,  $J = 8.9, 2.4$  Hz, 1H, H6 indole), 6.91–6.89 (m, 1H, CH pyrrole), 6.53–6.47 (m, 1H, CH pyrrole), 6.22–6.20 (m, 1H, CH pyrrole).  $^{13}\text{C}$  NMR (101 MHz, acetone- $d_6$ )  $\delta$  (ppm): 155.4, 138.7, 134.9, 131.1, 130.4, 130.3, 127.6, 124.8, 122.0, 119.3, 119.2, 118.0, 115.5, 115.0, 109.9, 109.8, 107.9, 107.8, 106.6.

#### Synthesis of 1-(phenylsulfonyl)-3-(1 H-pyrazol-4-yl)-1 H-indol-5-ol **21**

Compound **21** was synthesized according to general procedure B, starting from intermediate **15** (119.6 mg, 0.338 mmol, 1 eq) and 1 M  $\text{BBr}_3$  (2.0 mL) in dry DCM (3.4 mL) from  $-78^\circ\text{C}$  to  $0^\circ\text{C}$ , monitoring by TLC (eluent mixture: 7:3 n-hexane/EtOAc, developed in molybdc reagent). The crude was purified by column chromatography (eluent mixture: 6:4 n-hexane/EtOAc), affording 62.3 mg of pure compound **21** as a white solid (0.184 mmol, 54% yield). MS (ESI $^+$ ): 340.30  $[\text{M} + \text{H}]^+$ . Calculated MS for  $\text{C}_{17}\text{H}_{13}\text{N}_3\text{O}_3\text{S}$ : 339.07.  $^1\text{H}$  NMR (400 MHz, acetone- $d_6$ )  $\delta$  (ppm): 8.29 (s, 1H, OH), 7.98–7.91 (m, 2 H, CH phenyl-sulfonamide), 7.83 (d,  $J = 8.6$  Hz, 1H, H7 indole), 7.69–7.52 (m, 5 H, H2 indole, CH pyrazole, CH phenyl-sulfonamide), 6.98–6.93 (m, 1H, H4 indole), 6.92–6.84 (m, 1H, H6 indole), 6.68–6.62 (m, 1H, CH pyrazole).  $^{13}\text{C}$  NMR (101 MHz, acetone- $d_6$ )  $\delta$  (ppm) 155.0, 139.0, 135.0, 133.3, 130.3, 128.2, 127.6, 115.1, 114.7, 114.6, 110.3, 107.0, 106.9.

#### Synthesis of tert-butyl 2-(5-hydroxy-1-(phenylsulfonyl)-1 H-indol-3-yl)-1 H-pyrrole-1-carboxylate **20b**

$\text{Boc}_2\text{O}$  (311.0 mg, 1.425 mmol, 3 eq) and DMAP (2.3 mg, 0.019 mmol, 0.04 eq) were added to a stirred solution of compound **20a** (160.7 mg, 0.475 mmol, 1 eq) in dry DCM (9.5 mL) under nitrogen atmosphere and at room temperature. The reaction mixture was stirred for 3 h monitoring by TLC (eluent mixture: 7:3 n-hexane/EtOAc, developed in molybdc reagent). After reaction completion, the solution was washed with 1 M HCL (10 mL) and brine (10 mL). The organic phase was dried over sodium sulfate, filtered, and the solvent was removed under reduced pressure. The crude (241.3 mg) was then dissolved in DCM (3.5 mL) and piperidine (3.52 mL, 35.63 mmol, 75 eq) was added. The reaction mixture was stirred at room temperature for 6 h, monitoring by TLC (eluent mixture: 8:2 n-hexane/EtOAc, developed in molybdc reagent). Finally, the solution was washed with 1 M HCL (7 mL) and brine (7 mL). The organic phase was dried over sodium sulfate, filtered, and the solvent was removed under reduced pressure. The crude was purified by Biotage™ direct phase chromatography (cartridge: KPSIL 25 g, eluent mixture: n-hexane/EtOAc, gradient from 7 to 60% EtOAc) affording 126.9 mg of pure compound **20b** as a white solid (0.289 mmol, 61% yield). MS (ESI $^+$ ):  $m/z$  439.27  $[\text{M} + \text{H}]^+$ . Calculated MS for  $\text{C}_{23}\text{H}_{22}\text{N}_2\text{O}_5\text{S}$ : 438.12.  $^1\text{H}$  NMR (400 MHz, acetone- $d_6$ )  $\delta$  (ppm): 8.26 (bs, 1H, OH), 8.06–8.04 (m, 2 H, CH phenyl-sulfonamide), 7.88 (d,  $J = 7.9$  Hz, 1H, H7 indole), 7.70–7.68 (m, 1H, CH phenyl-sulfonamide), 7.68 (s, 1H, H1 indole), 7.67–7.60 (m, 2 H, CH phenyl-sulfonamide), 7.51 (s, 1H, CH pyrrole), 6.97 (d,  $J = 6.9$  Hz, 1H, H6 indole), 6.78 (s, 1H, H4 indole), 6.63 (s, 2 H, CH pyrrole), 1.01 (s, 9 H,  $\text{C}(\text{CH}_3)_3$ ).  $^{13}\text{C}$  NMR (101 MHz, acetone- $d_6$ )  $\delta$  (ppm): 148.9, 138.1, 134.5, 134.2, 132.9, 129.5, 128.6, 127.0, 126.9, 124.9, 122.9, 117.4, 115.4, 114.4, 113.9, 110.8, 105.5, 83.5, 26.2.



### General procedure C: IBX oxidation

IBX (1.2 eq) was added to a solution of phenol intermediates **16–19**, **20b** and **21** (1 eq) in DMF (0.17 M). The reaction mixture was stirred at room temperature and monitored by TLC (eluent mixture: 7:3 n-hexane/EtOAc, developed in molybdc reagent). After reaction completion (2 h), the mixture was diluted with distilled water and the aqueous phase was extracted three times with EtOAc. The collected organic phases were washed with brine, dried over sodium sulfate, and filtered. The crude was purified by flash chromatography or Biotage™ direct phase chromatography.

#### Synthesis of 1-(phenylsulfonyl)-3-(thiophen-2-yl)-1 H-indole-4,5-dione **3/TM9**

Compound **3 / TM9** was synthesized according to general procedure C, starting from intermediate **16** (99.7 mg, 0.280 mmol, 1 eq) and IBX (94.4 mg, 0.337 mmol, 1.2 eq) in DMF (1.7 mL). The crude was purified by column chromatography (eluent mixture: from 7:3 to 1:1 n-hexane/EtOAc), affording 87.4 mg of target **3 / TM9** (HPLC-MS purity > 95%) as a purple solid (0.237 mmol, 85% yield). MS (ESI<sup>+</sup>): m/z 370.27 [M + H]<sup>+</sup>. Calculated MS for C<sub>18</sub>H<sub>11</sub>NO<sub>4</sub>S<sub>2</sub>: 369.01. <sup>1</sup>H NMR (400 MHz, acetone-d<sub>6</sub>) δ (ppm): 8.28–8.21 (m, 2 H, CH phenyl-sulfonamide), 8.08 (d, J = 10.4 Hz, 1H, H7 indole), 7.97–7.84 (m, 3 H, CH phenyl-sulfonamide, H2 indole, CH thiophene), 7.82–7.73 (m, 2 H, CH phenyl-sulfonamide), 7.48 (dd, J = 5.1, 1.2 Hz, 1H, CH thiophene), 7.10 (dd, J = 5.1, 3.7 Hz, 1H, CH thiophene), 6.24 (d, J = 10.4 Hz, 1H, H6 indole). <sup>13</sup>C NMR (101 MHz, acetone-d<sub>6</sub>) δ (ppm): 136.7, 131.3, 131.2, 129.4, 128.5, 128.4, 127.3, 127.0, 123.5.

#### Synthesis of 1-(phenylsulfonyl)-3-(thiophen-3-yl)-1 H-indole-4,5-dione **4/TM10**

Compound **4 / TM10** was synthesized according to general procedure C, starting from intermediate **17** (85.9 mg, 0.290 mmol, 1 eq) and IBX (81.2 mg, 0.290 mmol, 1.2 eq) in DMF (1.4 mL). The crude was purified by column chromatography (eluent mixture: 6:4 n-hexane/EtOAc), affording 66.5 mg target **4 / TM10** (HPLC-MS purity ≈ 95%) as a purple solid (0.180 mmol, 74% yield). MS (ESI<sup>+</sup>): m/z 370.13 [M + H]<sup>+</sup>. Calculated MS for C<sub>18</sub>H<sub>11</sub>NO<sub>4</sub>S<sub>2</sub>: 369.01. <sup>1</sup>H NMR (400 MHz, acetone-d<sub>6</sub>) δ (ppm): 8.32 (dd, J = 3.0, 1.3 Hz, 1H, CH thiophene), 8.26–8.17 (m, 2 H, CH phenyl-sulfonamide), 8.07 (d, J = 10.5 Hz, 1H, H7 indole), 7.97 (s, 1H, H2 indole), 7.92–7.82 (m, 1H, CH phenyl-sulfonamide), 7.82–7.71 (m, 2 H, CH phenyl-sulfonamide), 7.61 (dd, J = 5.1, 1.3 Hz, 1H, CH thiophene), 7.49 (dd, J = 5.1, 3.0 Hz, 1H, CH thiophene), 6.22 (d, J = 10.4 Hz, 1H, H6 indole). <sup>13</sup>C NMR (101 MHz, acetone-d<sub>6</sub>) δ (ppm): 182.2, 174.9, 138.5, 137.9, 136.6, 132.4, 131.4, 131.3, 128.6, 128.5, 128.4, 127.0, 126.3, 125.9, 125.2, 124.3, 123.5.

#### Synthesis of 3-(furan-2-yl)-1-(phenylsulfonyl)-1 H-indole-4,5-dione **5/TM11**

Compound **5 / TM11** was synthesized according to general procedure C, starting from intermediate **18** (64.0 mg, 0.189 mmol, 1 eq) and IBX (63.4 mg, 0.226 mmol, 1.2 eq) in DMF (1.1 mL). The crude was purified by Biotage™ reverse phase chromatography (cartridge: KP-C18-HS (35–70 μm), 12 g, eluent mixture: CH<sub>3</sub>CN/H<sub>2</sub>O, gradient from 20 to 100% of CH<sub>3</sub>CN) affording 38.4 mg of target **5 / TM11** (HPLC-MS purity ≥ 99%) as a purple solid (0.109 mmol, 57% yield). MS (ESI<sup>+</sup>): m/z 354.17 [M + H]<sup>+</sup>. Calculated MS for C<sub>18</sub>H<sub>11</sub>NO<sub>5</sub>S: 353.04. <sup>1</sup>H NMR (400 MHz, acetone-d<sub>6</sub>) δ (ppm): 8.30–8.21 (m, 2 H, CH phenyl-sulfonamide), 8.07 (d, J = 10.5 Hz, 1H, H7 indole), 7.94–7.84 (m, 1H, CH phenyl-sulfonamide), 7.84 (s, 1H, H2 indole), 7.82–7.73 (m, 2 H, CH phenyl-sulfonamide), 7.62 (d, J = 1.8 Hz, 1H, CH furan), 7.55 (d, J = 3.4 Hz, 1H, CH furan), 6.55 (dd, J = 3.4, 1.8 Hz, 1H, CH furan), 6.24 (d, J = 10.5 Hz, 1H, H6 indole). <sup>13</sup>C NMR (101 MHz, acetone-d<sub>6</sub>) δ (ppm): 143.2, 136.7, 131.3, 131.1, 128.5, 126.9, 121.5, 112.8, 112.2.

#### Synthesis of 3-(furan-3-yl)-1-(phenylsulfonyl)-1 H-indole-4,5-dione **6/TM12**

Compound **6 / TM12** was synthesized according to general procedure C, starting from intermediate **19** (100.0 mg, 0.295 mmol, 1 eq) and IBX (99.0 mg, 0.354 mmol, 1.2 eq) in DMF (1.7 mL). The crude was purified by column chromatography (eluent mixture: 6:4 n-hexane/EtOAc), affording 80.6 mg of target **6 / TM12** (HPLC-MS purity ≈ 90%) as a red solid (0.228 mmol, 77% yield). MS (ESI<sup>+</sup>): m/z 354.17 [M + H]<sup>+</sup>. Calculated MS for C<sub>18</sub>H<sub>11</sub>NO<sub>5</sub>S: 353.04. <sup>1</sup>H NMR (400 MHz, acetone-d<sub>6</sub>) δ (ppm): 8.56 (d, J = 1.4 Hz, 1H, CH furan), 8.24–8.16 (m, 2 H, CH phenyl-sulfonamide), 8.07 (d, J = 10.5, 1H, H7 indole), 7.98 (s, 1H, H2 indole), 7.91–7.82 (m, 1H, CH phenyl-sulfonamide), 7.80–7.72 (m, 2 H, CH phenyl-sulfonamide), 7.61 (t, J = 1.8 Hz, 1H, CH furan), 7.05–6.99 (m, 1H, CH furan), 6.22 (d, J = 10.4 Hz, 1H, H6 indole). <sup>13</sup>C NMR (101 MHz, acetone-d<sub>6</sub>) δ (ppm): 182.0, 175.0, 144.2, 144.1, 138.5, 137.9, 136.6, 131.3, 128.4, 127.1, 123.7, 121.4, 117.4, 110.4.

#### Synthesis of tert-butyl 2-(4,5-dioxo-1-(phenylsulfonyl)-4,5-dihydro-1 H-indol-3-yl)-1 H-pyrrole-1-carboxylate **7b/TM13**

Compound **7b / TM13** was synthesized according to general procedure C, starting from intermediate **20b** (115.0 mg, 0.262 mmol, 1 eq) and IBX (73.4 mg, 0.262 mmol, 1 eq) in DMF (1.3 mL). The crude was purified by Biotage™ reverse phase chromatography (cartridge: KP-C18-HS (35–70 μm), 12 g, eluent mixture: CH<sub>3</sub>CN/H<sub>2</sub>O, gradient from 5 to 100% of CH<sub>3</sub>CN) affording 83.4 mg of target **7b/ TM13** (HPLC-MS purity ≈ 95%) as a red solid (0.184 mmol, 70% yield). MS (ESI<sup>+</sup>): m/z 353.0 [M + H]<sup>+</sup>. Calculated MS for C<sub>23</sub>H<sub>20</sub>N<sub>2</sub>O<sub>6</sub>S: 352.10. <sup>1</sup>H NMR (400 MHz, acetone-d<sub>6</sub>) δ (ppm): 8.25–8.23 (m, 2 H, CH phenyl-sulfonamide), 8.08 (d, J = 10.5, 1H, H7 indole), 7.91–7.87 (m, 1H, CH phenyl-sulfonamide), 7.80–7.75 (m, 2 H, CH phenyl-sulfonamide), 7.60 (s, 1H, H7 indole), 7.40 (t, J = 1.8 Hz, 1H, CH pyrrole), 7.28–6.18 (m, 3 H, CH pyrrole, H6 indole), 1.20 (s, 9 H, C(CH<sub>3</sub>)<sub>3</sub>). <sup>13</sup>C NMR (101 MHz, acetone-d<sub>6</sub>) δ (ppm): 181.5, 173.7, 148.6, 137.7, 135.7, 130.6, 130.4, 127.7, 127.6, 126.0, 124.8, 123.7, 123.1, 121.5, 115.2, 110.1, 83.2, 26.8.

## Biology

### *Cell line culture and treatment*

Murine macrophages RAW264.7 were cultivated in high glucose Dulbecco's modified Eagle's medium (DMEM) (Gibco, 11960-044) supplemented with 10% foetal bovine serum (FBS, Lonza, F4135), 2 mM L-glutamine (Gibco, 25030-024), 100 U/mL Penicillin–streptomycin (Gibco, 15070-063), in standard conditions. Cells were seeded 200,000 cells/mL. Cells were stimulated with LPS 1 µg/mL and either co-treated with TMs (10 µM) for 6 h, or stimulated for 2 h followed by addition of TMs and incubated 4 h.

### *RNA-electrophoretic mobility shift assays (REMSAs)*

A recombinant M1M2 version of HuR has been expressed in E.coli BL21 cells, as previously described<sup>21,41</sup>. REMSAs were performed as previously<sup>16</sup> to screen the binding-inhibition ability of the TMs. Briefly, the protein (3.7 nM) was incubated for 20 min with 5'-DY681-labelled AU-rich RNA probe (1 nM) and DMSO as control, or with TMs at different concentrations. Afterwards, samples were loaded on 4% native polyacrylamide gel and run for 1.5 h at 80 V; images were developed with a Typhoon Trio scanner (GE Healthcare) at the resolution for the DY681-probe (IR-short).

### *Homogeneous time resolved fluorescence (HTRF)*

M1M2 HuR recombinant protein was purified and HTRF was used to determine the inhibition of the binding between His-tag M1M2 HuR recombinant protein and a biotinylated TNF ARE RNA probe (5'-AUUAUUUAUUAUUUAUUUAUUUAUUUA-3') by the TM. The protein Hook point was calculated as previously described<sup>16</sup>. The recombinant protein (20 nM) was incubated with the RNA probe (50 nM), donor and acceptor beads and the TM. DMSO was used as control. HTRF experiments were performed according to the manufacturer instructions (Cisbio). The signals were measured with a Tecan Spark microplate reader, following the protocol indicated by the manufacturer (Cisbio).

### *Surface plasmon resonance (SPR)*

SPR experiments were carried out using a Biacore T200 instrument (GE Healthcare) using a CM5 chip with a carboxymethyl dextran surface (GE Healthcare). Recombinant M1M2 protein was immobilised on the chip surface using the standard amine coupling procedure according to the manufacturer's instructions. The chip surface was activated for 420 s with an *N*-ethyl-*N*-(3-dimethylaminopropyl)carbodiimide/*N*-hydroxysuccinimide solution using HBS buffer (10 mM HEPES, 150 mM NaCl, 0.05% Tween20, pH 7.5) and the protein was covalently immobilised to a final response of 7000 RU. The channel was then treated for 420 s with 1 M ethanolamine to block all unreacted groups. The blank channel was prepared the same way, only without treatment by any protein. Binding experiments were performed using running buffer (25 mM HEPES, pH 8, 3 mM MgCl<sub>2</sub>, 100 mM NaCl, 8% glycerol, 0.05% BSA, 0.005% Tween20, 1% DMSO). After chip equilibration, the studied compounds, were injected into the chip for 120 s in the running buffer at a flow rate of 30 µl/min at 25 °C. The injection was followed by 420 s of dissociation phase in running buffer that resulted in complete regeneration of the chip surface. To determine the apparent  $K_D$  towards the immobilised protein, we used the compounds in a concentration range of 1.56–25 µM. The differential curves (the blank channel response subtracted from the active channel) were evaluated with the evaluation software Biacore T200 using a steady state approach. Since the compounds were dissolved in DMSO, a separate injection of corresponding DMSO concentration was performed and the signal was subtracted from the signal of studied molecules. To determine the apparent  $K_D$  values, we fit the final data by 1:1 binding curve. Each experiment was performed in a tetraplicate and the final results were obtained as an average of individual fitted curves.

### *Enzyme-linked immunosorbent assays (ELISAs)*

ELISAs were performed on RAW 264.7 supernatant upon stimulation and treatment. supernatant was diluted 1:2. The procedure was performed according to the manufacturer instructions (R&D Systems, Mouse CXCL10/IP10/CRG-2 DUoSet ELISA #DY466). Signals were detected by using TMB solution (Thermo Fisher Scientific, N301) as substrate. Absorbance was read with a Tecan microplate reader at 605 nm.

### *Total RNA extraction and qRT-PCR*

Total RNA was extracted with Trizol, chloroform treatment and isopropanol precipitation. cDNA Synthesis was performed on RNA using RevertAid RT kit (Thermo Scientific, K1691) was performed from 500 ng of RNA, and qRT-PCRs were performed using Universal SYBR Master Mix (SMOBIO, TQ1201) on CFX-96 thermal cyclers (BIO-RAD). Normalised expression levels for each selected gene were calculated as  $2^{-\Delta\Delta Ct}$ , where the Ct value of either control or treatment conditions was subtracted from the Ct value of the housekeeping genes (RPLP0) to yield the  $\Delta Ct$  value. Then, the  $\Delta Ct$  value for treatment and control was calculated in triplicate and averaged to obtain one  $\Delta\Delta Ct$  value per sample.

### *Caspase 3/7 assay*

RAW 264.7 were seeded 50,000 cells/mL and co-treated for 48 h with 2 / **TM7n** or 5 / **TM11** and the CellEvent™ caspase-3/7 detection reagent. Pictures were acquired every 4 h by IncuCyte. Data were analysed with IncuCyte software. To assess Caspase 3 and PARP (full length and cleaved) levels, cells were treated for 48 h of exposure to TMs (15 µM) or the vehicle control (DMSO), and 4 h of incubation with staurosporin (1 µM) or staurosporin and QVD (10 µM). After that, cells were collected and lysed for 10 min on ice with RIPA lysis buffer (Merck, 20–188) supplemented with Protease Inhibitor Cocktail (ThermoScientific), followed by clarification. Protein content in each sample was quantified using the Pierce™ BCA Protein Assay (ThermoFisher Scientific, 23225). SDS-polyacrylamide gel was loaded with the same amounts of proteins. After, proteins were transferred to a

PVDF membrane, and the membrane was blocked with 5% milk solution in TBS buffer, and finally incubated with the primary antibodies. The primary antibodies used were: Caspase 3 (#9662, CST), PARP (#9542, CST) and  $\beta$ -actin (BK4970S CST).  $\beta$ -actin was used as protein loading control. The anti-rabbit secondary antibody (111-035-003) used was obtained from Jackson ImmunoResearch Laboratories. The signal was revealed with chemiluminescence detection kit reagents (Amersham ECL Select, GE Healthcare) at ChemiDoc (BioRad). A representative western blot is shown (Fig. 6E).

#### *Fluorescence-activated cell sorting (FACS)*

RAW 264.7 were seeded 250,000 cells/mL and treated for 48 h with **2** / **TM7n** or **5** / **TM11**. Starvation was performed for 24 h. Nocodazole treatment was performed for 2 h. Cells were fixed with ethanol 70% and stained with propidium iodide for fluorescence-activated cell sorting (FACS) analysis. Data were analysed and plotted with GraphPad Prism. Annexin V assay was performed using FITC Annexin V Apoptosis Detection Kit I (BD Pharmingen™). RAW 264.7 cells were seeded in a 6-well plate and treated for 48 h with **2** / **TM7n**, **5** / **TM11** or **MS-444** (15  $\mu$ M). Staurosporin (1  $\mu$ M) and co-treatment of staurosporin and QVD (10  $\mu$ M) were performed for 4 h, as apoptosis inducer and rescue controls, respectively. Cells were washed twice with PBS 1X and resuspended in 1X Annexin V Binding Buffer (component no. 51-66121E) at a concentration of  $1 \times 10^6$  cells/mL. 100  $\mu$ l of the solution was transferred to a 5 mL culture FACS tube and stained with 5  $\mu$ l of FITC Annexin V (component no. 51-65874X) and 5  $\mu$ l Propidium Iodide (PI) (component no. 51-66211E), for 15 min at room temperature. Stained cells were then analyzed by flow cytometry with BD FACSymphony™ A1 Cell Analyzer and analyzed with BD FACSDiva™ Software.

#### **Solubility measurement**

The solubility of **5** / **TM11** was measured according to a previous protocol<sup>16</sup>. Briefly, the compound (10 mM in DMSO) was mixed with aqueous buffers (PBS), with serial increase of the aqueous percentage. The samples were analysed at the LC-MS with the software Masslynx 4.0, processed with Microsoft Office Excel and plotted with GraphPad Prism.

#### **Quantum mechanics modelling of 3–6/TM9–12**

##### *Protein and TM compounds preparation*

All quantum-mechanics calculations on **3–6** / **TM9–12** were performed at B3LYP<sup>42</sup> 6–31 + G(d, p) theory level. Geometry optimizations and calculation of the electrostatic potentials were performed by taking into account the aqueous environment using the Conductor-like Polarizable Continuum Model (C-PCM). All calculations were performed using the Gaussian software (Gaussian 16: Revision A.03; Gaussian, Inc.: Wallingford, 2016). The mRNA model was built from the mRNA co-crystallized with HuR in the crystal structure (PDB Code: 4ED5<sup>14</sup>). In particular, the A7, U8, U9 were modelled, and dangling bonds were saturated with hydrogens. These nucleotides were chosen since they are the ones occupying almost the same binding region of **5** / **TM11** where U8 partially overlaps with it.

The crystallographic structure of HuR RRM1 and RRM2 complexed with mRNA (PDB code: 4ED5<sup>14</sup>) was chosen for the computational studies and prepared according to the following procedure by employing the graphical interface of the Schrödinger's molecular modelling platform, Maestro (Maestro, Schrödinger, LLC, New York, NY, 2021) v. 12.7.156. The module Protein Preparation Wizard<sup>43</sup>, Protein Preparation Wizard; Epik, Schrödinger, LLC, New York, NY, 2021; Impact, Schrödinger, LLC, New York, NY; Prime, Schrödinger, LLC, New York, NY, 2021) included in Maestro was used to add hydrogens, delete water molecules and cap the N- and C-terminal residues with the acetyl (ACE) and N-methyl amide (NME) groups, respectively. Finally, missing side chains were filled in by using the Prime (Prime, Schrödinger, LLC, New York, NY, 2021) module<sup>44,45</sup>. Then, to properly describe the protonation state of the protein residues and the hydrogen bonding networks correctly at neutral pH, the protonation states were assigned evaluating their pKa with the Propka program included in Maestro<sup>46</sup>. An inspection of histidines microenvironment was made, given the labile equilibrium at neutral pH of this residue, and none of them was considered protonated. Finally, a relaxation procedure was performed by running a restrained minimization only on the initially added hydrogen atoms according to the OPLS2005 force field<sup>47</sup>. **5** / **TM11** was prepared through the LigPrep (LigPrep, Schrödinger, LLC, New York, NY, 2021) module of Maestro, employing the OPLS2005 force field. Epik<sup>48,49</sup> (Epik, Schrödinger, LLC, New York, NY, 2021) was used to evaluate its pKa at neutral pH and so to properly describe its protonation state. The obtained ligand was further optimised at molecular mechanics level through the MacroModel (MacroModel, Schrödinger, LLC, New York, NY, 2021) program included in the Schrödinger suite of programs.

##### *Molecular docking simulations*

Molecular docking simulations were performed to achieve a molecular insight on the **5** / **TM11** interaction with the receptor. In particular, given the challenge of the HuR binding pocket due to its large and open shape, we decided to use two software i.e., Glide SP<sup>50–52</sup> (Schrödinger Release 2021-4: Glide, Schrödinger, LLC: New York, 2021) included in Maestro and Autodock4.2<sup>53</sup>.

In both cases, the choice of the receptor grid dimensions was based on the size of the binding region of mRNA and on the relative flexibility of the two HuR domains. In particular, a receptor grid of  $\sim 40 \text{ \AA} \times 40 \text{ \AA} \times 40 \text{ \AA}$  was generated centred on the native ligand centroid. Docking simulations with Glide were performed using default parameters. Sampling of nitrogen atoms inversions (when not belonging to cycles) and of different rings conformations were allowed, while non-planar amide conformations were penalised. The receptor was kept fixed, the ligand was treated as flexible, and no other constraints were added. Dockings' lowest energy poses converged in placing **5** / **TM11** in the same region, although through different spatial orientation of the different ligand moieties.

In docking simulations performed with Autodock4.2, a grid of the same size and settings to run docking calculations were prepared by using AutodockTools, the graphical interface of Autodock. The grid for docking calculations was computed by using  $108 \times 108 \times 108$  points, spaced by  $0.375 \text{ \AA}$ . These parameters correspond to a grid of  $\sim 40 \times \sim 40 \times \sim 40 \text{ \AA}$ , in agreement with the one used in Glide simulations. **5 / TM11** prepared with Maestro, was used for docking calculations. A hundred independent runs of the Lamarckian genetic algorithm local search method per docking calculations were performed and a threshold of maximum 25 million energy evaluations per run was applied. Docking conformations were clustered based on their RMSD (tolerance =  $2 \text{ \AA}$ ). The simulation gave two lowest energy poses populating two clusters, with the second pose populating the largest one. Both the poses were also found in docking simulations performed with Glide as the first and second lowest energy poses. The reliability of each pose was evaluated through two  $1.5 \mu\text{s}$  long molecular dynamics (MD) simulations.

#### Molecular dynamics simulations

The first and second lowest energy poses, the latter populating also the largest cluster, underwent  $1.5 \mu\text{s}$  MD simulations. In all cases the AMBER ff14SB<sup>54</sup> force field was employed for the protein, while the Generalized Amber Force Field (GAFF2<sup>55</sup>), was used for **5 / TM11**. RESP<sup>56</sup> atomic partial charges, obtained through the Antechamber accessory module of AmberTools, (AMBER 2018, University of California, San Francisco) were assigned to the ligand. In detail, ab-initio HF<sup>57</sup>/6-31G\* calculations were carried out with the revision A.03 of the Gaussian16 (Gaussian 16: Revision A.03; Gaussian, Inc.: Wallingford, 2016) software to compute the ESP<sup>58</sup> on optimized geometries of the ligands obtained at the density functional theory (DFT) level by employing the hybrid B3LYP<sup>42</sup> functional. Then, RESP charges were derived through the two-stages fitting procedure implemented in Antechamber.

The leap program available in AmberTools was used to prepare each complex for the MD simulations. In each system, a  $12 \text{ \AA}$  layer of TIP3P<sup>59</sup> water molecules were added, affording a box of about  $\sim 67 \text{ \AA} \times \sim 64 \text{ \AA} \times \sim 83 \text{ \AA}$ . The neutrality of the system was ensured by adding Cl<sup>-</sup> ions, modelled with Joung and Cheatham<sup>60,61</sup> parameters. Finally, coordinates and topology files for the whole system were obtained.

All the simulations were performed with Gromacs software<sup>62</sup>. The Verlet cut-off scheme was used for non-bonded interactions neighbour search, the smooth Particle-Mesh Ewald<sup>63</sup> (SPME) method was employed for long-range electrostatic interactions, while the cut-off for long-range Van der Waals interactions was set to  $1.2 \text{ nm}$ . The equilibration protocol consisted in energy minimization followed by subsequent NVT and NPT runs. The energy minimization consisted in two steps performed by using the steepest descent algorithm: (i) 20,000 steps, with harmonic restraints of  $1000 \text{ kJ mol}^{-1} \text{ nm}^{-2}$  applied to the ligand and the protein heavy atoms, so that only the solvent was unconstrained; and (ii) 20,000 steps during which the entire system was allowed to relax. Only for these runs, a gradual decrease in the Coulomb and Lennard-Jones potentials was imposed between  $1$  and  $1.2 \text{ nm}$ .

For all the MD simulations (either equilibration or production), the leap-frog<sup>64</sup> algorithm for integrating Newton's equations of motion was used and a time step of  $2 \text{ fs}$  was chosen, while the LINCS<sup>65</sup> algorithm was employed to constrain bonds involving hydrogen atoms. During the MD equilibration procedure, the system was gradually heated by increasing the temperature with subsequent MD runs in the canonical ensemble (NVT) using the weak-coupling Berendsen<sup>66</sup> scheme. In particular, three  $500 \text{ ps}$  NVT steps were performed by gradually increasing the temperature of  $100 \text{ K}$  up to  $300 \text{ K}$ . At each step, harmonic restraints were applied to all the heavy atoms of both the protein and the inhibitor, and were gradually decreased from  $1,000, 500$  to  $250 \text{ kJ mol}^{-1} \text{ nm}^{-2}$ . Then, two NPT equilibration runs of  $1$  and  $5 \text{ ns}$ , respectively, were performed to adjust the box volume, using the Berendsen algorithm for pressure coupling. In the first NPT step restraints of  $50 \text{ kJ mol}^{-1} \text{ nm}^{-2}$  were applied on heavy atoms, while no restraints were used in the last equilibration run.

For the  $1.5 \mu\text{s}$  production runs, temperature and pressure controls were carried-out with the velocity-rescale<sup>67</sup> and Parrinello-Rhman<sup>68</sup> scheme, respectively. All the trajectories visualization and RMSD analyses were carried out with the VMD (8744570<sup>69</sup>) software. All presented figures were obtained using ChimeraX<sup>70</sup> and the image manipulation program Gimp (2.10.22 revision 3), while the graphics were made with the Xmgrace (XMGRACE: version 5.1.19; Center for Coastal and Land-Margin Research, Oregon Graduate Institute of Science and Technology; Beaverton, 2005) software.

#### Data availability

The datasets used and/or analysed during the current study available from the corresponding author on reasonable request.

Received: 11 March 2024; Accepted: 16 September 2024

Published online: 18 October 2024

#### References

- Chaplin, D. D. Overview of the immune response. *J. Allergy Clin. Immunol.* **125**, S3–S23. <https://doi.org/10.1016/j.jaci.2009.12.980> (2010).
- Tucureanu, M. M. et al. Lipopolysaccharide-induced inflammation in monocytes/macrophages is blocked by liposomal delivery of G. *Int. J. Nanomed.* **13**, 63–76. <https://doi.org/10.2147/IJN.S150918> (2018).
- Ngkelo, A., Meja, K., Yeadon, M., Adcock, I. & Kirkham, P. A. LPS induced inflammatory responses in human peripheral blood mononuclear cells is mediated through NOX4 and G $\alpha$  dependent PI-3 kinase signalling. *J. Inflamm.* **9**, 1. <https://doi.org/10.1186/1476-9255-9-1> (2012).
- Tiedje, C. et al. The RNA-binding protein TTP is a global post-transcriptional regulator of feedback control in inflammation. *Nucleic Acids Res.* **44**, 7418–7440. <https://doi.org/10.1093/nar/gkw474> (2016).



5. Tiedje, C. et al. The p38/MK2-driven exchange between tristetraprolin and HuR regulates AU-rich element-dependent translation. *PLoS Genet.* **8**, e1002977. <https://doi.org/10.1371/journal.pgen.1002977> (2012).
6. Gueydan, C. et al. Identification of TIAR as a protein binding to the translational regulatory AU-rich element of tumor necrosis factor alpha mRNA. *J. Biol. Chem.* **274**, 2322–2326. <https://doi.org/10.1074/jbc.274.4.2322> (1999).
7. Ostareck, D. H. & Ostareck-Lederer, A. RNA-Binding proteins in the control of LPS-Induced Macrophage Response. *Front. Genet.* **10**, 31. <https://doi.org/10.3389/fgene.2019.00031> (2019).
8. Diaz-Muñoz, M. D. & Turner, M. Uncovering the role of RNA-Binding proteins in Gene expression in the Immune System. *Front. Immunol.* **9**, 1094. <https://doi.org/10.3389/fimmu.2018.01094> (2018).
9. Katsanou, V. et al. The RNA-binding protein Elavl1/HuR is essential for placental branching morphogenesis and embryonic development. *Mol. Cell. Biol.* **29**, 2762–2776. <https://doi.org/10.1128/MCB.01393-08> (2009).
10. Giammanco, A. et al. Intestinal epithelial HuR modulates distinct pathways of proliferation and apoptosis and attenuates small intestinal and colonic tumor development. *Cancer Res.* **74**, 5322–5335. <https://doi.org/10.1158/0008-5472.CAN-14-0726> (2014).
11. Yiakouvakis, A. et al. Myeloid cell expression of the RNA-binding protein HuR protects mice from pathologic inflammation and colorectal carcinogenesis. *J. Clin. Invest.* **122**, 48–61. <https://doi.org/10.1172/JCI45021> (2012).
12. Zucal, C. et al. Targeting the multifaceted HuR protein, benefits and caveats. *Curr. Drug Targets.* **16**, 499–515. <https://doi.org/10.2174/1389450116666150223163632> (2015).
13. Assoni, G. et al. HuR-targeted agents: an insight into medicinal chemistry, biophysical, computational studies and pharmacological effects on cancer models. *Adv. Drug Deliv. Rev.* **181**, 114088. <https://doi.org/10.1016/j.addr.2021.114088> (2022).
14. Wang, H. et al. The structure of the ARE-binding domains of Hu antigen R (HuR) undergoes conformational changes during RNA binding. *Acta Crystallogr. D Biol. Crystallogr.* **69**, 373–380. <https://doi.org/10.1107/S0907444912047828> (2013).
15. Rajasingh, J. The many facets of RNA-binding protein HuR. *Trends Cardiovasc. Med.* **25**(8), 684–686. <https://doi.org/10.1016/j.tcm.2015.03.013> (2015).
16. Bonomo, I. et al. HuR modulation counteracts lipopolysaccharide response in murine macrophages. *Dis. Model. Mech.* **16**, dmm.050120 (2023). <https://doi.org/10.1242/dmm.050120>
17. Liu, S. et al. Inhibition of RNA-binding protein HuR reduces glomerulosclerosis in experimental nephritis. *Clin. Sci.* **134**, 1433–1448. <https://doi.org/10.1042/CS20200193> (2020).
18. Majumder, M., Chakraborty, P., Mohan, S., Mehrotra, S. & Palanisamy, V. HuR as a molecular target for cancer therapeutics and immune-related disorders. *Adv. Drug Deliv. Rev.* **188**, 114442. <https://doi.org/10.1016/j.addr.2022.114442> (2022).
19. Muralidharan, R. et al. Folate receptor-targeted nanoparticle delivery of HuR-RNAi suppresses lung cancer cell proliferation and migration. *J. Nanobiotechnol.* **14**, 47. <https://doi.org/10.1186/s12951-016-0201-1> (2016).
20. Manzoni, L. et al. Interfering with HuR-RNA Interaction: Design, synthesis and Biological characterization of Tanshinone Mimics as Novel, effective HuR inhibitors. *J. Med. Chem.* **61**, 1483–1498. <https://doi.org/10.1021/acs.jmedchem.7b01176> (2018).
21. D'Agostino, V. G. et al. Dihydrotanshinone-I interferes with the RNA-binding activity of HuR affecting its post-transcriptional function. *Sci. Rep.* **5**, 16478. <https://doi.org/10.1038/srep16478> (2015).
22. Meisner, N. C. et al. Identification and mechanistic characterization of low-molecular-weight inhibitors for HuR. *Nat. Chem. Biol.* **3**, 508–515. <https://doi.org/10.1038/nchembio.2007.14> (2007).
23. Wu, X. et al. Identification and validation of novel small molecule disruptors of HuR-mRNA interaction. *ACS Chem. Biol.* **10**, 1476–1484. <https://doi.org/10.1021/cb500851u> (2015).
24. Wu, X. et al. Targeting the interaction between RNA-binding protein HuR and FOXQ1 suppresses breast cancer invasion and metastasis. *Commun. Biol.* **3**, 193. <https://doi.org/10.1038/s42003-020-0933-1> (2020).
25. Wu, X. & Xu, L. The RNA-binding protein HuR in human cancer: A friend or foe? *Adv. Drug Deliv. Rev.* **184**, 114179 (2022).
26. Jampilek, J. Heterocycles in medicinal chemistry. *Molecules.* **24**, 3839. <https://doi.org/10.3390/molecules24213839> (2019).
27. Mathis, G. HTRF(R) technology. *J. Biomol. Screen.* **4**, 309–314. <https://doi.org/10.1177/108705719900400605> (1999).
28. Degorce, F. et al. HTRF: A technology tailored for drug discovery—A review of theoretical aspects and recent applications. *Curr. Chem. Genom.* **3**, 22–32. <https://doi.org/10.2174/1875397300903010022> (2009).
29. Branko, S. J. Suitability of furan, pyrrole and thiophene as dienes for Diels–Alder reactions viewed through their stability and reaction barriers for reactions with acetylene, ethylene and cyclopropene. An AM1 semiempirical and B3LYP hybrid density functional theory study. *J. Mol. Struct. Theochem.* **454**, 105–116. [https://doi.org/10.1016/S0166-1280\(98\)00281-4](https://doi.org/10.1016/S0166-1280(98)00281-4) (1998).
30. Horner, K. E. & Karadakov, P. B. Chemical bonding and aromaticity in furan, pyrrole, and thiophene: A magnetic shielding study. *J. Org. Chem.* **78**, 8037–8043. <https://doi.org/10.1021/jo401319k> (2013).
31. Kim, H. S. et al. Different modes of interaction by TIAR and HuR with target RNA and DNA. *Nucleic Acids Res.* **39**, 1117–1130. <https://doi.org/10.1093/nar/gkq837> (2011).
32. Piotr, C. An ab initio study on nucleic acid bases aromaticities. *J. Mol. Struct. Theochem.* **714**, 29–34. <https://doi.org/10.1016/j.theochem.2004.10.030> (2005).
33. Taro, U. Theoretical analysis on the aromaticity of uracil: Important electronic configurations and solvent effect on the aromaticity. *Chem. Phys. Lett.* **637**, 115–119. <https://doi.org/10.1016/j.cplett.2015.07.057> (2015).
34. Wang, W., Caldwell, M. C., Lin, S., Furneaux, H. & Gorospe, M. HuR regulates cyclin A and cyclin B1 mRNA stability during cell proliferation. *EMBO J.* **19**, 2340–2350. <https://doi.org/10.1093/emboj/19.10.2340> (2000).
35. Osmá-García, I. C. et al. The RNA-binding protein HuR is required for maintenance of the germinal centre response. *Nat. Commun.* **12**, 6556. <https://doi.org/10.1038/s41467-021-26908-2> (2021).
36. Muralidharan, R. et al. HuR-targeted small molecule inhibitor exhibits cytotoxicity towards human lung cancer cells. *Sci. Rep.* <https://doi.org/10.1038/s41598-017-07787-4> (2017).
37. Krishnamurthy, P. et al. IL-10 inhibits inflammation and attenuates left ventricular remodeling after myocardial infarction via activation of STAT3 and suppression of HuR. *Circ. Res.* **104**, e9–e18. <https://doi.org/10.1161/CIRCRESAHA.108.188243> (2009).
38. Zhou, C. et al. ELAVL1 promotes LPS-induced endothelial cells injury through modulation of cytokine storm. *Immunobiology.* **228**, 152412. <https://doi.org/10.1016/j.imbio.2023.152412> (2023).
39. Katsanou, V. et al. HuR as a negative posttranscriptional modulator in inflammation. *Mol. Cell.* **19**, 777–789. <https://doi.org/10.1016/j.molcel.2005.08.007> (2005).
40. Christodoulou-Vafeiadou, E. et al. Divergent innate and epithelial functions of the RNA-Binding protein HuR in intestinal inflammation. *Front. Immunol.* **9**, 2732. <https://doi.org/10.3389/fimmu.2018.02732> (2018).
41. Lal, P. et al. Regulation of HuR structure and function by dihydrotanshinone-I. *Nucleic Acids Res.* **45**, 9514–9527. <https://doi.org/10.1093/nar/gkx623> (2017).
42. Becke, A. D. Density-functional thermochemistry. III. The role of exact exchange. *J. Chem. Phys.* **98**, 5648–5652. <https://doi.org/10.1063/1.464913> (1993).
43. Sastry, G. M., Adzhigirey, M., Day, T., Annabhimoju, R. & Sherman, W. Protein and ligand preparation: Parameters, protocols, and influence on virtual screening enrichments. *J. Comput. Aided Mol. Des.* **27**, 221–234. <https://doi.org/10.1007/s10822-013-9644-8> (2013).
44. Jacobson, M. P. et al. A hierarchical approach to all-atom protein loop prediction. *Proteins.* **55**, 351–367. <https://doi.org/10.1002/prot.10613> (2004).
45. Jacobson, M. P., Friesner, R. A., Xiang, Z. & Honig, B. On the role of the crystal environment in determining protein side-chain conformations. *J. Mol. Biol.* **320**, 597–608. [https://doi.org/10.1016/S0022-2836\(02\)00470-9](https://doi.org/10.1016/S0022-2836(02)00470-9) (2002).

46. Olsson, M. H., Søndergaard, C. R., Rostkowski, M. & Jensen, J. H. PROPKA3: Consistent treatment of Internal and Surface residues in empirical pK<sub>a</sub> predictions. *J. Chem. Theory Comput.* **7**, 525–537. <https://doi.org/10.1021/ct100578z> (2011).
47. Banks, J. L. et al. Integrated modeling program, applied chemical theory (IMPACT). *J. Comput. Chem.* **26**, 1752–1780. <https://doi.org/10.1002/jcc.20292> (2005).
48. Greenwood, J. R., Calkins, D., Sullivan, A. P. & Shelley, J. C. Towards the comprehensive, rapid, and accurate prediction of the favorable tautomeric states of drug-like molecules in aqueous solution. *J. Comput. Aided Mol. Des.* **24**, 591–604. <https://doi.org/10.1007/s10822-010-9349-1> (2010).
49. Shelley, J. C. et al. Epik: A software program for pK(a) prediction and protonation state generation for drug-like molecules. *J. Comput. Aided Mol. Des.* **21**, 681–691. <https://doi.org/10.1007/s10822-007-9133-z> (2007).
50. Friesner, R. A. et al. Extra precision glide: Docking and scoring incorporating a model of hydrophobic enclosure for protein-ligand complexes. *J. Med. Chem.* **49**, 6177–6196. <https://doi.org/10.1021/jm051256o> (2006).
51. Friesner, R. A. et al. Glide: A new approach for rapid, accurate docking and scoring. 1. Method and assessment of docking accuracy. *J. Med. Chem.* **47**, 1739–1749. <https://doi.org/10.1021/jm0306430> (2004).
52. Halgren, T. A. et al. Glide: A new approach for rapid, accurate docking and scoring. 2. Enrichment factors in database screening. *J. Med. Chem.* **47**, 1750–1759. <https://doi.org/10.1021/jm030644s> (2004).
53. Morris, G. M. et al. AutoDock4 and AutoDockTools4: Automated docking with selective receptor flexibility. *J. Comput. Chem.* **30**, 2785–2791. <https://doi.org/10.1002/jcc.21256> (2009).
54. Maier, J. A. et al. ff14SB: Improving the Accuracy of protein side chain and backbone parameters from ff99SB. *J. Chem. Theory Comput.* **11**, 3696–3713. <https://doi.org/10.1021/acs.jctc.5b00255> (2015).
55. Wang, J., Wolf, R. M., Caldwell, J. W., Kollman, P. A. & Case, D. A. Development and testing of a general amber force field. *J. Comput. Chem.* **25**, 1157–1174. <https://doi.org/10.1002/jcc.20035> (2004).
56. Bayly, C., Cieplak, P., Cornell, W. & Kollman, P. A. A well-behaved electrostatic potential based method using charge restraints for deriving atomic charges: The RESP model. *J. Phys. Chem.* **97**, 10269–10280. <https://doi.org/10.1021/j100142a004> (1993).
57. Roothaan, C. C. J. New developments in molecular orbital theory. *Rev. Mod. Phys.* **23**, 69. <https://doi.org/10.1103/RevModPhys.23.69> (1951).
58. Gordon, J. C., Fenley, A. T. & Onufriev, A. An analytical approach to computing biomolecular electrostatic potential. II. Validation and applications. *J. Chem. Phys.* **129**, 075102. <https://doi.org/10.1063/1.2956499> (2008).
59. Jorgensen, W. L., Chandrasekhar, J., Madura, J. D., Impey, R. W. & Klein, M. L. Comparison of simple potential functions for simulating liquid water. *J. Chem. Phys.* **79**, 926–935. <https://doi.org/10.1063/1.445869> (1983).
60. Joung, I. S. & Cheatham, T. E. Determination of alkali and halide monovalent ion parameters for use in explicitly solvated biomolecular simulations. *J. Phys. Chem. B.* **112**, 9020–9041. <https://doi.org/10.1021/jp8001614> (2008).
61. Joung, I. S. & Cheatham, T. E. Molecular dynamics simulations of the dynamic and energetic properties of alkali and halide ions using water-model-specific ion parameters. *J. Phys. Chem. B.* **113**, 13279–13290. <https://doi.org/10.1021/jp902584c> (2009).
62. Bekker, H. et al. GROMACS—A Parallel Computer for Molecular-Dynamics Simulations. (World Sci. Publishing, 1993), 252–256.
63. Essmann, U. et al. A smooth particle mesh Ewald method. *J. Chem. Phys.* **103**, 8577–8593. <https://doi.org/10.1063/1.470117> (1995).
64. Hockney, R. W., Goel, S. P. & Eastwood, J. W. Quiet high-resolution computer models of a plasma. *J. Computat Phys.* **14**, 148–158. [https://doi.org/10.1016/0021-9991\(74\)90010-2](https://doi.org/10.1016/0021-9991(74)90010-2) (1974).
65. Hess, B. et al. A linear constraint solver for molecular simulations. *J. Computat Chem.* **18**, 1463–1472. [https://doi.org/10.1002/\(SICI\)1096-987X\(199709\)18:12%3C1463::AID-JCC4%3E3.0.CO;2-H](https://doi.org/10.1002/(SICI)1096-987X(199709)18:12%3C1463::AID-JCC4%3E3.0.CO;2-H) (1998).
66. Berendsen, H. J. C., Postma, J. P. M., van Gunsteren, W. F., DiNola, A. & Haak, J. R. Molecular dynamics with coupling to an external bath. *J. Chem. Phys.* **81**, 3684–3690. <https://doi.org/10.1063/1.448118> (1984).
67. Bussi, G., Donadio, D. & Parrinello, M. Canonical sampling through velocity rescaling. *J. Chem. Phys.* **126**, 014101. <https://doi.org/10.1063/1.2408420> (2007).
68. Parrinello, M. & Rahman, A. Polymorphic transitions in single crystals: A new molecular dynamics method. *J. Appl. Phys.* **52**, 7182–7190. <https://doi.org/10.1063/1.328693> (1981).
69. Humphrey, W., Dalke, A. & Schulten, K. VMD: Visual molecular dynamics. *J. Mol. Graph.* **14**, 33–38. [https://doi.org/10.1016/0263-7855\(96\)00018-5](https://doi.org/10.1016/0263-7855(96)00018-5) (1996).
70. Pettersen, E. F. et al. UCSF ChimeraX: Structure visualization for researchers, educators, and developers. *Protein Sci.* **30**, 70–82. <https://doi.org/10.1002/pro.3943> (2021).

## Acknowledgements

This work was supported by Associazione Italiana per la Ricerca sul Cancro (IG 21548 to A.P.), Fondazione Pezcoller (to E.F.), ‘Integrata’ H2020 Marie Skłodowska-Curie Actions Innovative Training Networks (ITN) (813284), PNRR-MUR NextGenerationEU cod. CN00000041- to L.M., and the Ministero della Salute Italiano GR2019-12369266. We acknowledge CF BIC of CIISB, Instruct-CZ Centre, supported by MEYS CR (LM2023042) and European Regional Development Fund-Project „UP CIISB“ (No. CZ.02.1.01/0.0/0.0/18\_046/0015974).

## Author contributions

E.F. prepared and produced data in Figs. 3, 6, and 7, drafted and finalized the manuscript. G.A. prepared and produced data in Figs. 1 and 2, and Scheme 1. G.D., V.L.P. prepared and produced data in Figs. 4 and 5. D.P., A.C., L.F., I.B., R.L., J.H., contributed to data in Figs. 3, 6, and 7. L.M., P.S., D.A., A.P., supervised, managed the project and finalized the manuscript. G.A., D.A., P.S., L.M., and A.P. ideated the work. All authors reviewed the manuscript.

## Declarations

## Competing interests

The authors declare no competing interests.

## Additional information

**Supplementary Information** The online version contains supplementary material available at <https://doi.org/10.1038/s41598-024-73309-8>.

**Correspondence** and requests for materials should be addressed to L.M., D.A. or A.P.

**Reprints and permissions information** is available at [www.nature.com/reprints](http://www.nature.com/reprints).

**Publisher's note** Springer Nature remains neutral with regard to jurisdictional claims in published maps and institutional affiliations.

**Open Access** This article is licensed under a Creative Commons Attribution-NonCommercial-NoDerivatives 4.0 International License, which permits any non-commercial use, sharing, distribution and reproduction in any medium or format, as long as you give appropriate credit to the original author(s) and the source, provide a link to the Creative Commons licence, and indicate if you modified the licensed material. You do not have permission under this licence to share adapted material derived from this article or parts of it. The images or other third party material in this article are included in the article's Creative Commons licence, unless indicated otherwise in a credit line to the material. If material is not included in the article's Creative Commons licence and your intended use is not permitted by statutory regulation or exceeds the permitted use, you will need to obtain permission directly from the copyright holder. To view a copy of this licence, visit <http://creativecommons.org/licenses/by-nc-nd/4.0/>.

© The Author(s) 2024